

PAPER • OPEN ACCESS

ITER materials irradiation within the D–T neutron environment at JET: post-irradiation radioactivity analysis following the DTE2 experimental campaign









To cite this article: L.W. Packer *et al* 2024 *Nucl. Fusion* **64** 106059

View the [article online](#) for updates and enhancements.

You may also like

- [Physics basis for the divertor tokamak test facility](#)
F. Crisanti, R. Ambrosino, M.V. Falessi et al.
- [Density profiles in stellarators: an overview of particle transport, fuelling and profile shaping studies at TJ-II](#)
J.A. Alonso, D. Alegre, J. Alonso et al.
- [The core–edge integrated neon-seeded scenario in deuterium–tritium at JET](#)
C. Giroud, I.S. Carvalho, S. Brezinsek et al.

ITER materials irradiation within the D–T neutron environment at JET: post-irradiation radioactivity analysis following the DTE2 experimental campaign

L.W. Packer^{1,*} , P. Batistoni², C. Bearcroft¹, S.C. Bradnam¹, E. Eardley¹, M. Fabbri⁵ , N. Fonesu² , M.R. Gilbert¹ , Z. Ghani¹, K. Gorzkiewicz³, C.L. Grove¹, R. Kierepko³, E. Łaszyńska⁴, I. Lengár⁸, X. Litaudon⁶ , S. Loreti², J.W. Mietelski³, M. Pillon² , M.I. Savva⁷ , C.R. Shand¹ , I.E. Stamatelatos⁷, A.N. Turner¹, T. Vasilopoulou⁷, R. Villari², A. Wójcik-Gargula³, A. Žohar⁸ and JET Contributors^a

¹ United Kingdom Atomic Energy Authority, Culham Campus, Abingdon, Oxon OX14 3DB, United Kingdom of Great Britain and Northern Ireland

² ENEA—Department of Fusion and Technology for Nuclear Safety and Security via E. Fermi 45,44 Frascati (Rome), Italy

³ Institute of Nuclear Physics, Polish Academy of Sciences, 31-342 Krakow, Poland

⁴ Institute of Plasma Physics and Laser Microfusion, 01-497 Warsaw, Poland

⁵ Fusion for Energy, Josep Pla 2, Torres Diagonal Litoral B3, 8019 Barcelona, Spain

⁶ CEA, IRFM, F-13108 Saint-Paul-lez-Durance, France

⁷ Institute of Nuclear and Radiological Sciences, Technology, Energy and Safety, NCSR Demokritos, Athens 15310, Greece

⁸ Reactor Physics Department, Jožef Stefan Institute, Jamova cesta 39, SI-1000 Ljubljana, Slovenia

E-mail: lee.packer@ukaea.uk

Received 2 January 2024, revised 6 August 2024

Accepted for publication 14 August 2024

Published 13 September 2024



CrossMark

Abstract

This work presents the results following the first irradiation of ITER materials samples in a tokamak D–T plasma environment operating at significant fusion power. The materials exposed to this nuclear environment at the Joint European Torus during the DTE2 experimental campaign that took place in 2021 include representative ITER samples from various components such as poloidal field coil jacket samples, toroidal field coil radial closure plate steels, EUROFER 97 steel, W and CuCrZr materials from the divertor, Inconel-718 and 316L stainless steel for blanket modules, as well as vacuum vessel forging samples. The experimental results discussed include high-resolution gamma spectrometry measurements and analysis conducted with the post-irradiated samples, of which there were 68 in total. These samples were exposed

^a See Maggi *et al* 2024 (<https://doi.org/10.1088/1741-4326/ad3e16>) for JET Contributors.

* Author to whom any correspondence should be addressed.



Original Content from this work may be used under the terms of the [Creative Commons Attribution 4.0 licence](https://creativecommons.org/licenses/by/4.0/). Any further distribution of this work must maintain attribution to the author(s) and the title of the work, journal citation and DOI.

through different experimental campaigns, including deuterium, deuterium–tritium and tritium phases. Diagnostics that supported the analysis included 25 dosimetry foil-based neutron diagnostics and two ‘VERDI’ neutron spectrometry diagnostics. A further 12 samples for positron annihilation spectroscopy were also irradiated. The irradiation of all these samples took place in a long-term irradiation assembly located near the JET vacuum vessel. The post-irradiation analysis of the ITER material samples has yielded valuable insights into their material activation levels and radiation fields. Comparative assessments between experimental measurements and comprehensive neutronics simulations have demonstrated a significant level of agreement in this work, while also revealing some discrepancies in specific material instances. The data and interpretation from this work not only serve as a robust experimental foundation for enhancing the precision and predictability of neutronics simulation approaches for ITER and next-step devices but also present some opportunities for the refinement of simulation methodologies. In light of these findings, a series of recommendations have been proposed, aimed at improving confidence in nuclear predictions associated with materials that have been exposed to fusion nuclear environments and advancing understanding in this important domain.

Keywords: neutronics, activation, ITER, JET, gamma spectrometry

(Some figures may appear in colour only in the online journal)

1. Introduction

Experiments at the Joint European Torus (JET) during the 2021 D–T (DTE2) experimental campaign produced 59 MJ of fusion energy [1] whilst demonstrating sustained plasma operations in a tokamak device. The unique nuclear environment at JET, characterised by the production of neutrons born in the plasma with energies around 14.1 MeV, and the opportunities to learn from these operations through irradiation and radiation transport-related studies are of significant relevance to ITER. Some of the materials used within ITER are expected to be exposed to high neutron fluxes, reaching up to approximately $2 \times 10^{14} \text{ n cm}^{-2} \text{ s}^{-1}$ at first wall (FW) armour locations, during the foreseen 500 MW fusion power operations. In comparison, the highest instantaneous neutron flux seen at JET at the long-term irradiation station (LTIS)—the location relevant to the irradiation analysis that we describe in this paper—was estimated to be approximately $2 \times 10^{13} \text{ n cm}^{-2} \text{ s}^{-1}$ during the 59 MJ plasma discharge (shot 99971). Whilst only one order of magnitude lower in terms of flux, the total neutron fluence during the whole DTE2 experimental campaign for samples contained within the LTIS ranged from $4.86\text{--}5.10 \times 10^{15} \text{ n cm}^{-2}$, significantly lower fluence than the total neutron fluence expected to be achieved at first wall locations at ITER of $\sim 3.4 \times 10^{21} \text{ n cm}^{-2}$ over the planned 14 year of D–T operations. However, the experimental work we discuss in this paper has provided the opportunity to test the latest nuclear modeling (neutronics) predictions against measurements of the neutron-induced activation of ITER material samples performed in a highly relevant tokamak environment with the highest 14.1 MeV neutron yield and exposure to date. New and unique experimental measurements have been performed with detailed analysis following the irradiation during the DTE2 and C40 tritium campaigns, performed using samples of structural materials used in manufacturing the main ITER tokamak components. Sensitive

radiometric techniques deployed across five European laboratories (ENEA, IFJ PAN, IPPLM, NCSR D and UKAEA) have been used to study 27 different ITER material samples irradiated in this environment. These were analysed post-irradiation using high-resolution gamma spectrometers to allow accurate quantification of the levels of neutron-induced activation with quantified radionuclide contributions. The activities, initiated under the EUROfusion JET3 project (2015–2020) and building on previous work [2–5], are continuing with new activities within the scope of the Preparation of ITER Operation (PrIO) programme’s Neutronics, Nuclear waste and Safety subtask. Significant recent results obtained to date have a focus on relevance to ITER device operations [6–9], including activation measurements, the 14 MeV calibration of neutron yield monitors [10–12], neutronics benchmark experiments [13–19], nuclear diagnostics and data processing for tritium breeding blankets [20, 21]. Furthermore, 14 MeV accelerator-based neutron sources, such as the Frascati Neutron Generator (FNG) in Italy [22], the Fusion Neutron Source (FNS) in Japan [23], and the ASP facility in the UK [24], have advanced the understanding of fusion neutron transport, shielding, and related neutron-material interaction phenomena. These contributions, along with validation, verification, and benchmark activities [25, 26], have further underpinned the neutronics simulation methodologies deployed in this work.

The experimental results presented in this paper include gamma spectrometry measurements and analysis obtained following the DTE2 campaigns, where samples (see original materials, from which subsamples were taken in figure 1) were irradiated over 715 days in a long-term irradiation station (LTIS) assembly (see figure 2) in a location very close to the JET vacuum vessel, outside of the vacuum boundary. The samples were extracted following their irradiation and then distributed to five European laboratories for gamma spectrometry analysis to identify the radionuclides present

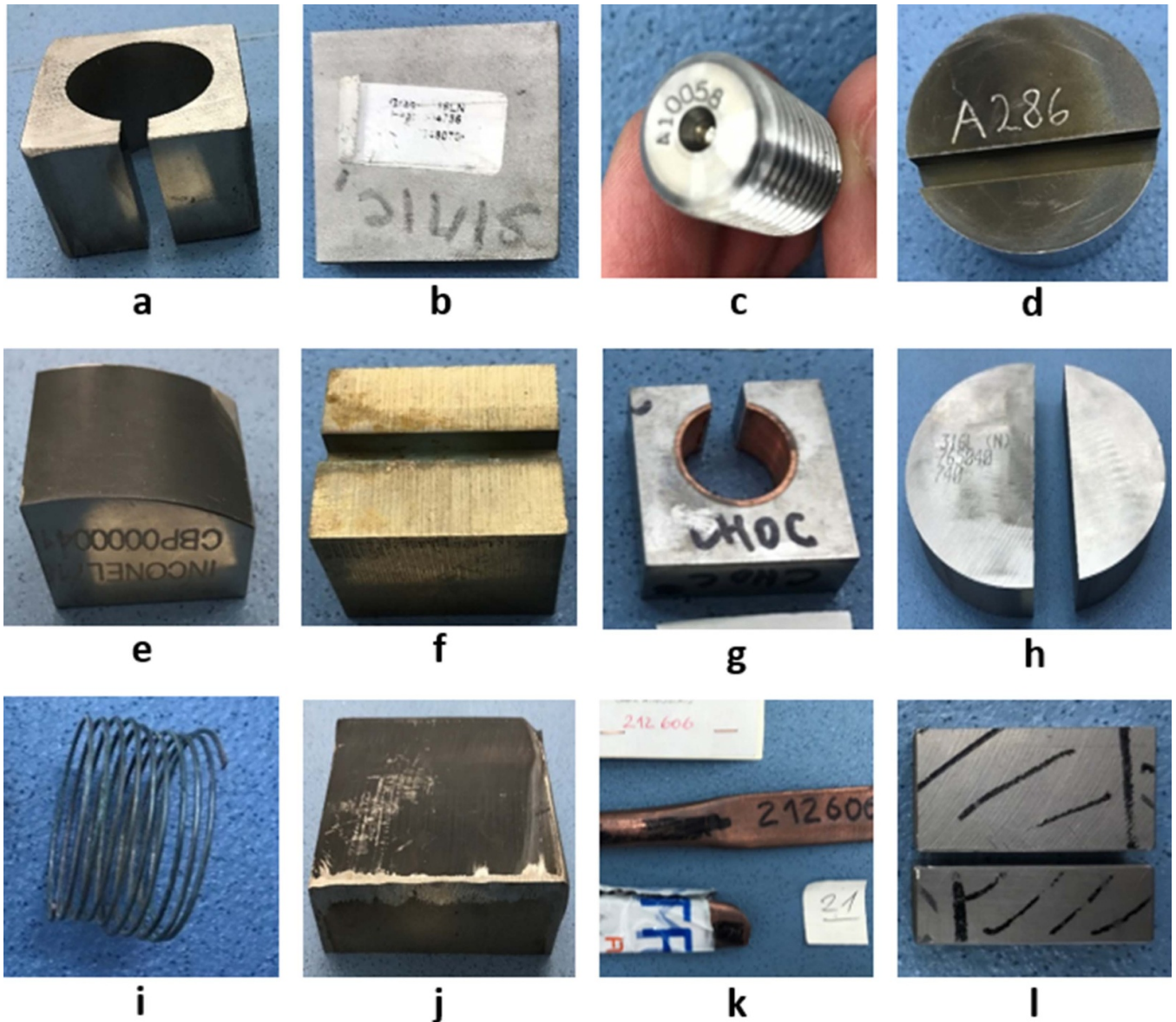


Figure 1. Selected ITER material samples: (a) PF coil jacket; (b) radial closure plate for TF coil; (c) TF coil case specimen; (d) in-wall shielding material; (e) Inconel 718; (f) divertor material; (g) divertor W monoblock; (h) vacuum vessel forging; (i) reacted TF strand; (j) vacuum vessel plate; (k) CuCrZr pipes for the divertor; (l) EUROFER-97 material. Reproduced from [3]. © EURATOM 2018. All rights reserved.

and accurately determine their activity. A complete set of measurement results is presented in this paper and compared with corresponding calculations using the FISPACT-II inventory code [27, 28] with ITER material compositions linked with neutron spectra derived from recent MCNP radiation transport calculations [29] performed using a detailed JET model containing the LTIS, material sample geometry and material compositions.

2. Specification of ITER materials, sample loading and irradiation configuration

This section describes inputs to the experimental irradiation of samples within the JET environment. These include details,

such as the elemental specification of the ITER material samples and dosimetry foils, sample loading arrangements and irradiation configuration. Additionally, details of the gamma spectrometry systems, their calibration and the associated analysis methodologies adopted are provided.

A range of ITER materials from various manufacturers and used for different ITER components were sourced by Fusion for Energy (F4E). They include samples from the poloidal field (PF) coil jacket and toroidal field coil radial closure plate steels, EUROFER 97-2 steel, W and CuCrZr materials from the divertor, 304 stainless steel, XM-19, Inconel 718 and 316 L stainless steel for blanket modules and vacuum vessel forging samples (see figure 1 and table 1). The materials, related identifiers and sources have previously been detailed in [2]. These bulk materials were shipped to UKAEA in various forms

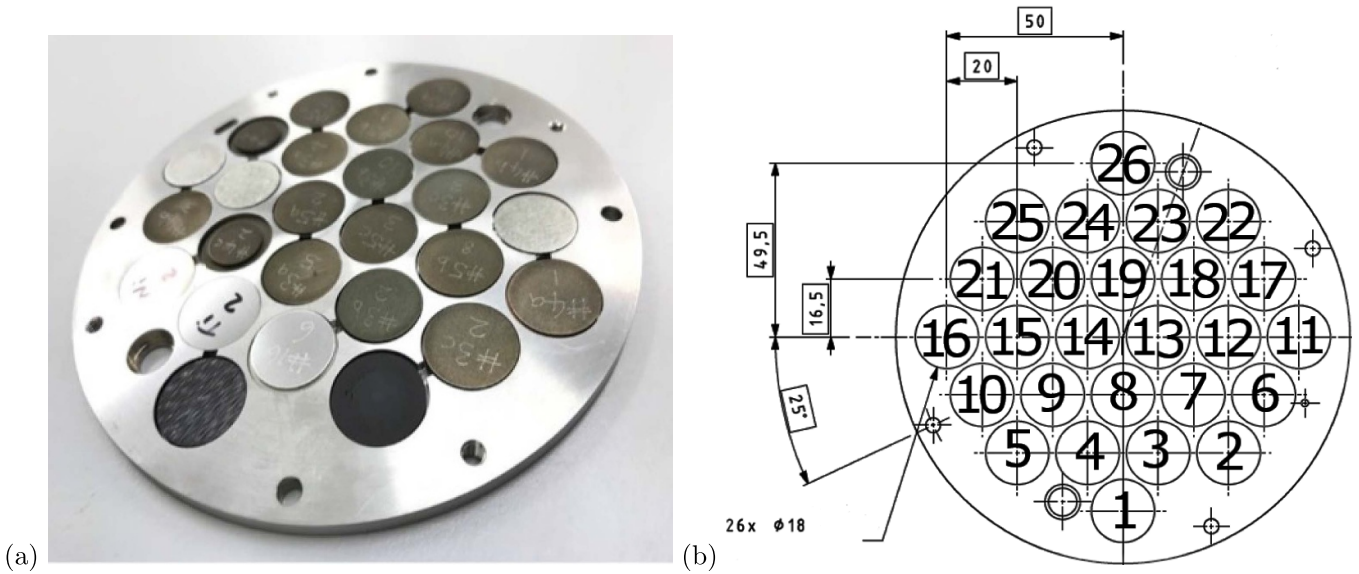


Figure 2. (a) Photograph of the fully-loaded LTIS assembly holder containing the samples prior to irradiation; (b) drawing showing the sample holder position numbers and key physical dimensions in mm.

and prepared by UKAEA's Special Techniques Group using electrical discharge machining (EDM) to cut disc samples that were also uniquely etched (labelled). The accompanying elemental composition analysis certificates, alongside those defined in [30, 31], have been used as input to the series of inventory simulation output results provided in section 5.

A total of 68 ITER material samples, 25 dosimetry foil-based neutron diagnostics, together with two VERDI [32] detectors and 12 samples for positron annihilation spectroscopy (PALS) were installed in an assembly holder machined from 304 stainless steel, which comprises 26 sample cavity positions (see figure 3). Each cavity within the assembly holder is 2 mm deep and can accommodate multiple samples up to 18 mm in diameter. The samples were not physically separated from each other using additional spacing materials. The dosimetry foils provide an absolute neutron fluence measurement at the irradiation position within JET. The post-irradiation PALS sample analysis is not included in this paper but is expected to be reported separately. Figure 3 shows an image of the assembly and the numbering scheme associated with the 26 channel positions. The installation of this assembly, within a long-term irradiation station (LTIS) into octant 7 of the JET machine, was completed on the 4th October 2020. The first neutron exposure at JET of the assembly following the installation was on the 8th October 2020 (shot 98020, within a JET D–D campaign).

3. Post-irradiation sample retrieval, distribution and analysis method for samples

The LTIS assembly containing the samples was retrieved on 25th September 2022, with the last neutron exposure prior to retrieval of the LTIS on 23rd September 2022 (shot 101175).

The contact gamma dose rate on 13th October 2022 from the bulk LTIS assembly (predominantly due to the steel in the assembly cassette, which is approximately 0.7 kg) was measured to be $660 \mu\text{Sv h}^{-1}$ using a Ludlum Model 26-1 instrument. The assembly holder was transferred to the Materials Research Facility (MRF) active fume cupboard as minor drilling operations were required to remove the assembly cover plate, as the thermal cycling of the assembly during irradiation distorted the threads and led to difficulties in removing the stainless steel screws holding the plate in place. Based on this experience, a recommendation was made for the irradiation of samples in the more recent DTE3 experimental campaign at JET to replace these screws with aluminium bronze-coated screws. The post-irradiation analysis from the DTE3 experimental campaign is ongoing and is expected to be reported as part of a future contribution from this scientific collaboration.

The samples were extracted from the cassette in an active area set up at the MRF. Some samples were then shipped for subsequent high-resolution gamma spectrometry measurements at several European laboratories: ENEA, IFJ PAN, IPPLM, and NCSRD, whilst the remaining were kept for analysis at UKAEA. Each laboratory reported results, which included the measured sample mass, identified radionuclides, decay-corrected activity, and measurement uncertainty. The methodology for calibration, analysis and reporting of activity results, illustrated in the following section, were similar across each of the laboratories with some differences, such as the HPGe instrument specifications.

Figure 4 shows an example of the plastic sample mounting jig (left-hand side image) and measurement system used at UKAEA, which comprises a broad-energy Germanium (BEGe) detector with a Compton Suppression System (CSS, see middle image). The BEGe (model BE3825) has a relative

Table 1. ITER material description, unique LTIS position ID and other relevant details for irradiated samples exposed during the JET irradiation campaign. The sample LTIS position–depth ID may be used to map to the LTIS configuration shown in figure 2 and 3.

Sample LTIS position_depth ID	Material	Manufacturer and sample details
1_1, 1_4, 13_4	SS316L(N)-IG	Industeel Groupe Arcelor, ITER vacuum vessel plate
1_2, 13_2, 18_1	EUROFER 97-2	Saarschmiede Gmbh, Vacuum Induction Melting (VIM) + Vacuum Arc Remelting (VAR) 1.4914x3 EUROFER 97-2, order no: 8186 097
1_3, 13_3	Alloy 660 (Divertor)	Copper Alloys Ltd, ITER divertor material
2_1, 2_4, 14_4	SS316L(N)-IG	R. Kind GmBh, ITER vacuum vessel plate
2_2, 14_2	EUROFER 97-2	Saarschmiede GmbH, Vacuum Induction Melting (VIM) + Vacuum Arc Remelting (VAR) 1.4914x3, EUROFER 97-2, order no: 8186 097
2_3, 14_3	Alloy 660 (Divertor)	Copper Alloys Ltd, ITER divertor material
3_1, 3_4, 15_4	SS316L(N)-IG	Thyssen Krupp Materials France SAS, forged block ITER grade vacuum vessel plate, specimen number 5939
3_2, 15_2, 19_1	Al–Bronze	Aubert & Duval, used for the ITER inner vertical target (IVT), Copper Alloys Ltd Cast ID: 51 519 051
3_3, 7_1, 15_3	CuCrZr	Yamato, First wall component, divertor pipe 212 601
4_1, 4_4, 16_4	SS316L(N)	Thyssen Krupp Materials France SAS, Radial plates (jacket) for the ITER toroidal field coils (2500/64)
4_2, 16_2	Al–Bronze	Aubert & Duval, For the ITER inner vertical target (IVT), Cast ID: 51 519 051
4_3, 16_3	CuCrZr	KME, First wall component, divertor pipe 212 606
5_1, 5_4, 17_4	SS316(N)	Thyssen Krupp Materials France SAS, Radial plates for the ITER toroidal field coils, 316LN Class C2 solution treated and quenched, stress relieved (2500/68)
5_2, 17_2, 20_1	SS304(IWS)	Carpenter powder products, India DA, ITER In-wall shield sample (IWS), Heat Nr 5600 413
5_3, 8_1, 17_3	Tungsten	AT&M for ATMOSTAT, W monoblocks, purity 99.5, ref: PD-13 482-999
6_1, 6_4, 18_4	SS316L(N)	Thyssen Krupp Materials France SAS, Radial plates for the ITER toroidal field coils, 316LN Class C2 solution treated and quenched, stress relieved (2501/33)
6_2, 18_2	SS304(IWS)	Carpenter powder products, India DA, In-wall shield sample (IWS)
6_3, 18_3	Tungsten	AT&M for ATMOSTAT, W monoblocks, purity 99.5, ref: PD-13 482-999
7_2, 19_2	SS316L	Salzgitter Mannesmann Stainless Tubes GmbH, Poloidal field coil jacket
7_3, 9_1, 19_3	XM-19	Aubert & Duval, Forgings for divertor cassette
7_4, 19_4	SS316L(N)	SIMIC-CNIM Consortium, Special TF cover plate (304 757)
8_2, 20_2, 21_1	Alloy 660 (IWS)	Villares Metals, ITER In wall shield (IWS) A286
8_3, 20_3	XM-19	Aubert & Duval, Forgings for the ITER divertor cassette
8_4, 20_4	SS316L(N)	SIMIC-CNIM Consortium, Special TF cover plate (304 761)
9_2, 21_2	SS316L	Outokumpu, Divertor Nadege 316L
9_3, 17_1, 21_3	Inconel 718	Aubert & Duval, Inconel alloy 718
9_4, 21_4	SS316L(N)	SIMIC-CNIM Consortium, Special TF cover plate (304 756)

efficiency to a 3×3 inch NaI detector of 26% and an energy resolution of 1.69 keV full-width half maximum at a photon energy of 1.33 MeV. The CSS has an array of NaI-based guard detectors (manufactured by Scionix) used as an anti-coincidence shield. The entire system is housed in substantial shielding comprising Pb with thin Sn and Cu layers to reduce background x-rays. The BEGe with CSS electronics is configured using three Lynx multi-channel analysers (the gate delay, input gate delay, and gate width parameters were set at $0 \mu\text{s}$, $6.2 \mu\text{s}$, $1 \mu\text{s}$, respectively). Data is recorded and analysed using Genie2000 software with post-processing and plotting enabled using UKAEA's neutronics toolkit software.

Each participating laboratory utilised high-resolution gamma spectrometry instruments to capture emission spectra from the samples; these instruments, with varying specifications, have been comprehensively described in a prior work [2]. Detector energy and efficiency calibration was typically

accomplished using mixed radionuclide calibration sources or LabSOCS software with traceable validation. UKAEA's approach for calibrating the broad-energy Germanium detector (BEGe) and Compton suppression system (CSS) involved generating sample-specific photopeak efficiency data as a function of energy via LabSOCS. Preceding measurement, the HPGe detector underwent energy calibration using a certified mixed radionuclide source (AG5430) issued by Deutschen Kalibrierdienst (DKD). This source encompasses gamma-emitting radionuclides, spanning energies from 59 keV to 1836 keV, including ^{57}Co , ^{60}Co , ^{109}Cd , ^{137}Cs , and ^{241}Am . The relative activity uncertainty of these radionuclides is 3% (except for ^{109}Cd with 5%) at $k = 2$. An assessment of this source occurred on 10th October 2022, employing the BEGe detector and a configuration consisting of the BEGe detector surrounded by 7 NaI detectors, used to veto Compton scattering events and other related coincident phenomena.

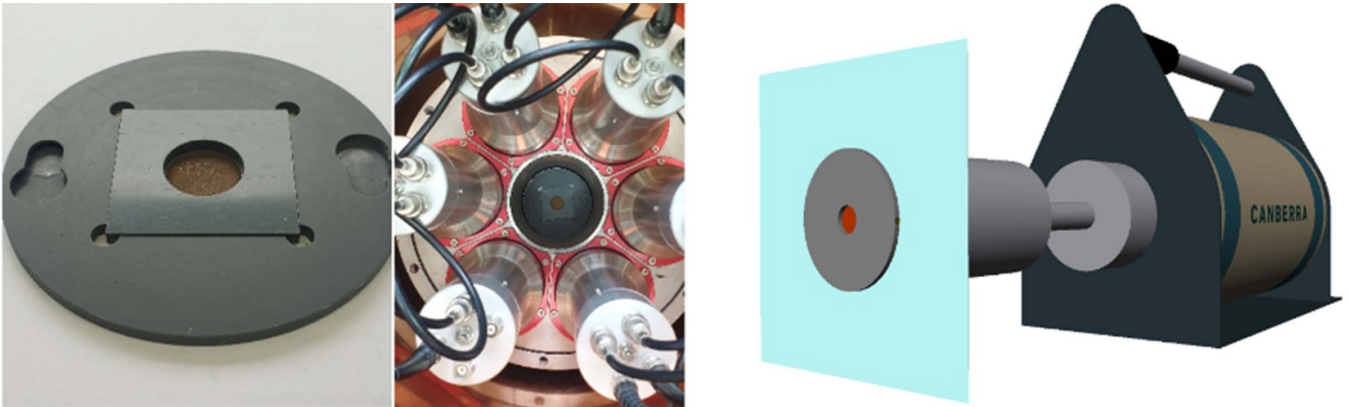


Figure 4. (LHS) Sample positioned in the plastic holder; (Middle) Sample in the measurement position above the BEGe detector. The BEGe and sample are surrounded by 7 NaI-based detectors (6 are seen in this photo, with a 7th removable detector that would be positioned in the central cavity above the sample prior to acquisition commencing), which comprises the Compton suppression shield; (RHS) Image representing the ISOCS geometry of sample, used to generate photopeak efficiency data.

4. Post-irradiation radioactivity analysis using gamma spectrometry techniques

This section provides details of the JET post-irradiation radioactivity analysis using gamma spectrometry techniques, example gamma energy spectra and a comprehensive table of specific activity results for radionuclides associated with each irradiated sample.

The decay-corrected specific activity measurements for 16 individual radionuclides across all analysed ITER material samples, as measured by participating laboratories, are presented in tables 2 and 3. Figure 5 highlights illustrative gamma energy spectra obtained from sample measurements conducted by UKAEA. These spectra facilitate the identification and quantification of isotopes and their activity within each sample. Notably, the black and red lines correspond to gamma spectra captured with and without the Compton suppression system (CSS) respectively. The analysis of these particular materials are highlighted within this paper because they include some notable results that differ from our computational analysis (discussed further in section 6), and also because their gamma spectra effectively demonstrate some of the key capabilities of the CSS, as outlined in this section.

Figure 5(a) depicts a spectrum from an irradiated tungsten monoblock sample (LTIS position ID 5_3, fabricated by Atmosstat, ALCEN-Group-France). This spectrum, acquired over a live time of 2.75 days, distinctly displays characteristic lines attributed to isotopes such as ^{54}Mn , ^{57}Co , ^{58}Co , ^{60}Co , ^{65}Zn , ^{182}Ta , ^{181}Hf , ^{181}W , and ^{185}W . Live time accounts for processing time where the detector is not responsive to other incoming gamma-ray events, generally known as dead time. Detector live time is the difference between the real-time as measured by a clock and the dead time. The material analysis certificate from AT&M specifies that the Fe and Ni content in the sample is 0.0002 wt% and <0.0005 wt%, respectively. Further details on activities related to the manufacturing and procurement of the ITER divertor target can be found in works such as [33].

Figure 5(b) presents a spectrum from an irradiated CuCrZr sample (LTIS position ID 3_3, manufactured by Yamato, Japan) acquired over a live time of 1 day. This spectrum reveals distinct lines corresponding to ^{51}Cr , ^{54}Mn , ^{57}Co , ^{58}Co , ^{60}Co , ^{65}Zn , ^{95}Zr , ^{95}Nb , $^{110\text{m}}\text{Ag}$, and ^{182}Ta . The materials certificate reported Co, Nb, and Ta content, each below 0.003 wt%, determined through ICP-OES, with the total impurity level below 0.15 wt%.

Some peaks in both spectra are not directly attributable to radionuclide peaks; for example, the 511 keV annihilation peak, characteristic x-rays from the Pb shield, naturally occurring radioactive material (NORM) peaks, escape peaks, and multiple sum peaks, many of which originate from ^{182}Ta , along with the ^{60}Co sum peak at approximately 2505 keV (some of these have been labelled in the figure).

The spectra comparison demonstrate that employing the CSS significantly increases the signal-to-background ratio for some radionuclides, enabling the identification of some challenging-to-measure isotopes that might otherwise remain elusive to identification through conventional gamma spectrometry methods. Compton suppression is an advanced gamma spectrometry analysis technique that enhances the accuracy and sensitivity of radionuclide identification [34]. The Compton scattering process, where gamma rays interact with a detector or external material, scattering and losing energy, creates a background continuum in the energy spectrum; this can obscure the peaks of some specific radionuclides. The CSS addresses this issue by incorporating a primary high-purity germanium (HPGe) detector surrounded by a secondary detector array comprising scintillators such as NaI(Tl) detectors in the case of the system used in this work. When a gamma ray undergoes Compton scattering and interacts with the primary detector and one or more secondary detectors within a short time window, the system registers this as a scattering event. By identifying and rejecting (vetoing) these coincident scattering events, the system effectively reduces the Compton background in the energy spectrum. This suppression of the Compton continuum enhances the peak-to-background ratio,

Table 2. First summary table of the gamma spectrometry results from all laboratories. Measured specific activities for the radionuclides listed have been decay corrected to 21/12/2021 21:53 (the end of the DTE2 campaign) with $k = 2$ expanded uncertainties reported. Sample Pos. ID refers to the foil location within the LTIS in the form *channel_depth*, i.e. sample position ID 1_3 represents the third position in channel 1.

Lab	Sample Pos. ID	Material	Radionuclide Activity (Bq g ⁻¹)									
			⁴⁶ Sc	⁵¹ Cr	⁵⁴ Mn	⁵⁹ Fe	⁵⁶ Co	⁵⁷ Co	⁵⁸ Co	⁶⁰ Co		
UKAEA	1_1	SS316L(N)-IG	—	(1.95 ± 0.16) × 10 ³	(5.39 ± 0.32) × 10 ³	514 ± 22	—	(9.04 ± 0.50) × 10 ³	(2.66 ± 0.09) × 10 ⁴	198 ± 6		
	14_4	SS316L(N)-IG	—	(1.90 ± 0.15) × 10 ⁵	(5.34 ± 0.32) × 10 ³	436 ± 21	—	(9.06 ± 0.50) × 10 ³	(2.69 ± 0.09) × 10 ⁴	171 ± 5		
	15_4	SS316L(N)-IG	—	(1.80 ± 0.15) × 10 ⁵	(5.51 ± 0.33) × 10 ³	490 ± 19	—	(8.79 ± 0.48) × 10 ³	(2.63 ± 0.08) × 10 ⁴	217 ± 6		
	16_4	SS316L(N)	—	(1.93 ± 0.16) × 10 ⁵	(5.14 ± 0.31) × 10 ³	438 ± 24	—	(8.64 ± 0.47) × 10 ³	(2.66 ± 0.09) × 10 ⁴	167 ± 5		
	5_1	SS316L(N)	—	(1.97 ± 0.16) × 10 ⁵	(5.48 ± 0.33) × 10 ³	484 ± 24	—	(9.25 ± 0.51) × 10 ³	(2.73 ± 0.09) × 10 ⁴	181 ± 5		
	1_3	Alloy 660 (Divertor)	328 ± 12	(1.70 ± 0.14) × 10 ⁵	(4.49 ± 0.27) × 10 ³	512 ± 30	—	(1.83 ± 0.10) × 10 ⁴	(5.32 ± 0.17) × 10 ⁴	468 ± 13		
	3_3	CuCrZr	—	(8.83 ± 0.78) × 10 ³	1.24 ± 0.13	—	—	3.06 ± 0.22	25.48 ± 1.89	783 ± 22		
	4_3	CuCrZr	—	(7.23 ± 0.69) × 10 ³	—	—	—	0.37 ± 0.04	—	765 ± 22		
	5_3	Tungsten	—	—	0.29 ± 0.02	—	—	2.07 ± 0.21	1.47 ± 0.16	0.94 ± 0.03		
	7_3	XM-19	—	(2.35 ± 0.19) × 10 ⁵	(9.65 ± 0.58) × 10 ³	427 ± 16	—	(8.79 ± 0.48) × 10 ³	(2.56 ± 0.08) × 10 ⁴	181 ± 5		
	8_3	XM-19	—	(2.26 ± 0.18) × 10 ⁵	(9.41 ± 0.57) × 10 ³	456 ± 17	—	(8.46 ± 0.46) × 10 ³	(2.53 ± 0.08) × 10 ⁴	178 ± 5		
	21_3	Inconel-718	139 ± 8	(1.81 ± 0.15) × 10 ⁵	958 ± 57	529 ± 19	—	(4.14 ± 0.22) × 10 ⁴	(1.14 ± 0.04) × 10 ⁵	665 ± 19		
	1_2	Eurofer 97-2	—	(1.07 ± 0.09) × 10 ⁵	(4.87 ± 0.29) × 10 ³	702 ± 26	—	14.25 ± 1.03	41.37 ± 2.84	7.50 ± 0.25		
	2_2	Eurofer 97-2	—	(1.09 ± 0.09) × 10 ⁵	(5.02 ± 0.30) × 10 ³	774 ± 30	—	11.51 ± 0.88	30.40 ± 2.59	7.27 ± 0.25		
3_2	Al-Bronze	—	—	455 ± 27	—	—	(4.04 ± 0.22) × 10 ³	(1.09 ± 0.04) × 10 ⁴	707 ± 20			
20_1	SS304 (IWS)	—	(1.96 ± 0.16) × 10 ⁵	(4.24 ± 0.25) × 10 ³	496 ± 19	—	(9.53 ± 0.52) × 10 ³	(2.74 ± 0.09) × 10 ⁴	186 ± 5			
8_2	Alloy 660 (IWS)	343 ± 12	(1.61 ± 0.13) × 10 ⁵	(4.64 ± 0.28) × 10 ³	509 ± 19	—	(1.93 ± 0.10) × 10 ⁴	(5.57 ± 0.17) × 10 ⁴	312 ± 9			
NCSRD	13_4	SS316L(N)-IG	—	—	(4.20 ± 0.25) × 10 ³	—	—	(9.09 ± 0.38) × 10 ³	(2.52 ± 0.15) × 10 ⁴	168 ± 7		
	2_4	SS316L(N)-IG	—	—	(5.28 ± 0.31) × 10 ³	—	—	(1.01 ± 0.04) × 10 ⁴	(2.79 ± 0.16) × 10 ⁴	199 ± 8		
	3_4	SS316L(N)-IG	—	—	(5.55 ± 0.32) × 10 ³	—	—	(1.08 ± 0.08) × 10 ⁴	(2.80 ± 0.16) × 10 ⁴	250 ± 10		
	4_4	SS316L(N)	—	—	(5.26 ± 0.31) × 10 ³	—	—	(1.00 ± 0.04) × 10 ⁴	(2.67 ± 0.16) × 10 ⁴	194 ± 8		
	17_4	SS316L(N)	—	—	(5.08 ± 0.30) × 10 ³	—	—	(9.82 ± 0.41) × 10 ³	(2.67 ± 0.16) × 10 ⁴	199 ± 8		
	18_4	SS316L(N)	—	—	(4.87 ± 0.28) × 10 ³	—	—	(9.74 ± 0.40) × 10 ³	(2.71 ± 0.16) × 10 ⁴	193 ± 8		
	13_3	Alloy 660 (Divertor)	341 ± 23	—	(4.57 ± 0.27) × 10 ³	—	—	(2.02 ± 0.08) × 10 ⁴	(5.61 ± 0.33) × 10 ⁴	526 ± 22		
	2_3	Alloy 660 (Divertor)	289 ± 15	—	(4.52 ± 0.26) × 10 ³	—	—	(2.01 ± 0.08) × 10 ⁴	(5.57 ± 0.27) × 10 ⁴	540 ± 22		
	8_1	Tungsten	—	—	—	—	—	—	—	2.14 ± 0.17		
	18_3	Tungsten	—	—	—	—	—	2.17 ± 0.36	—	6.71 ± 0.66		
	19_3	XM-19	—	—	(9.10 ± 0.53) × 10 ³	—	—	—	(2.53 ± 0.15) × 10 ⁴	193 ± 8		
	17_1	Inconel-718	188 ± 16	—	983 ± 57	—	—	(4.53 ± 0.19) × 10 ⁴	(1.20 ± 0.05) × 10 ⁵	796 ± 33		
	13_2	Eurofer 97-2	—	—	(4.89 ± 0.29) × 10 ³	—	—	10.75 ± 1.03	—	10.01 ± 0.47		
	17_2	SS304 (IWS)	—	—	(4.17 ± 0.24) × 10 ³	—	—	(1.02 ± 0.04) × 10 ⁴	(2.79 ± 0.16) × 10 ⁴	214 ± 9		
18_2	SS304 (IWS)	—	—	(4.10 ± 0.24) × 10 ³	—	—	(1.00 ± 0.04) × 10 ⁴	(2.68 ± 0.16) × 10 ⁴	209 ± 9			
19_2	SS316L	—	—	(5.43 ± 0.32) × 10 ³	—	—	(9.91 ± 0.41) × 10 ³	(2.75 ± 0.16) × 10 ⁴	209 ± 9			
21_2	SS316L	—	—	(5.02 ± 0.29) × 10 ³	—	—	(9.39 ± 0.39) × 10 ³	(2.47 ± 0.14) × 10 ⁴	205 ± 8			

(Continued.)

Table 2. (Continued.)

Lab	Sample Pos. ID	Material	Radionuclide Activity (Bq g ⁻¹)							
			⁴⁶ Sc	⁵¹ Cr	⁵⁴ Mn	⁵⁹ Fe	⁵⁶ Co	⁵⁷ Co	⁵⁸ Co	⁶⁰ Co
ENEА	3_1	SS316L(N)-IG	—	—	(5.10 ± 0.15) × 10 ³	—	—	(8.90 ± 0.42) × 10 ³	(2.57 ± 0.08) × 10 ⁴	233 ± 2
	6_1	SS316L(N)	—	—	(2.71 ± 0.08) × 10 ³	—	—	(4.88 ± 0.22) × 10 ³	(1.41 ± 0.04) × 10 ⁴	102 ± 4
	7_4	SS316L(N)	—	—	(4.21 ± 0.12) × 10 ³	—	—	(8.64 ± 0.41) × 10 ³	(2.51 ± 0.07) × 10 ⁴	192 ± 5
	20_4	SS316L(N)	—	—	(4.14 ± 0.12) × 10 ³	—	—	(8.51 ± 0.40) × 10 ³	(2.48 ± 0.07) × 10 ⁴	192 ± 5
	9_4	SS316L(N)	—	—	(4.11 ± 0.12) × 10 ³	—	—	(8.49 ± 0.40) × 10 ³	(2.48 ± 0.07) × 10 ⁴	189 ± 4
	14_3	Alloy 660 (Divertor)	—	—	(4.14 ± 0.12) × 10 ³	—	—	(1.74 ± 0.07) × 10 ⁴	(5.07 ± 0.15) × 10 ⁴	474 ± 10
	9_1	XM-19	—	—	(8.51 ± 0.25) × 10 ³	—	—	(8.19 ± 0.42) × 10 ³	(2.38 ± 0.07) × 10 ⁴	182 ± 4
	20_3	XM-19	—	—	(8.45 ± 0.25) × 10 ³	—	—	(8.13 ± 0.38) × 10 ³	(2.36 ± 0.07) × 10 ⁴	178 ± 4
	9_3	Inconel-718	—	—	889 ± 25	—	—	(3.87 ± 0.18) × 10 ⁴	(1.14 ± 0.03) × 10 ⁵	709 ± 15
	15_2	Al-Bronze	—	—	374 ± 12	—	—	(3.21 ± 0.15) × 10 ³	(9.23 ± 0.28) × 10 ³	668 ± 14
	16_2	Al-Bronze	—	—	370 ± 12	—	—	(3.16 ± 0.14) × 10 ³	(9.01 ± 0.27) × 10 ³	657 ± 14
	6_2	SS304 (IWS)	—	—	(3.75 ± 0.11) × 10 ³	—	—	(8.84 ± 0.41) × 10 ³	(2.52 ± 0.07) × 10 ⁴	191 ± 4
	20_2	Alloy 660 (IWS)	—	—	(4.20 ± 0.12) × 10 ³	—	—	(1.81 ± 0.08) × 10 ⁴	(5.22 ± 0.15) × 10 ⁴	322 ± 7
	9_2	SS316L	—	—	(4.79 ± 0.14) × 10 ³	—	—	(8.62 ± 0.40) × 10 ³	(2.51 ± 0.07) × 10 ⁴	192 ± 4
15_3	CuCrZr	—	—	—	—	—	—	—	815 ± 17	
16_3	CuCrZr	—	—	—	—	—	—	—	805 ± 17	
14_2	Eurofer 97-2	—	—	(2.42 ± 0.07) × 10 ³	—	—	—	—	3.50 ± 0.30	
IFJ PAN	5_4	SS316L(N)	—	(1.57 ± 0.30) × 10 ⁵	(4.07 ± 0.41) × 10 ³	443 ± 100	168 ± 18	(8.09 ± 0.81) × 10 ³	(2.19 ± 0.23) × 10 ⁴	163 ± 16
	6_4	SS316L(N)	—	(1.75 ± 0.92) × 10 ⁵	(4.08 ± 0.44) × 10 ³	670 ± 213	106 ± 17	(8.27 ± 0.89) × 10 ³	(2.25 ± 0.30) × 10 ⁴	163 ± 18
	19_4	SS316L(N)	—	(1.36 ± 0.25) × 10 ⁵	(3.47 ± 0.35) × 10 ³	462 ± 94	165 ± 17	(7.99 ± 0.80) × 10 ³	(2.12 ± 0.22) × 10 ⁴	167 ± 17
	21_4	SS316L(N)	—	(1.44 ± 0.24) × 10 ⁵	(3.42 ± 0.34) × 10 ³	361 ± 70	126 ± 13	(7.91 ± 0.79) × 10 ³	(2.10 ± 0.22) × 10 ⁴	167 ± 17
	7_1	CuCrZr	—	(7.70 ± 1.74) × 10 ⁴	1.64 ± 0.54	—	—	3.67 ± 0.94	24.70 ± 8.62	735 ± 74
	6_3	Tungsten	—	(2.47 ± 0.57) × 10 ⁵	0.20 ± 0.10	—	—	—	—	1.00 ± 0.13
	18_1	Eurofer 97-2	—	(2.10 ± 1.27) × 10 ⁵	(5.83 ± 0.63) × 10 ³	690 ± 291	157 ± 22	(1.18 ± 0.13) × 10 ⁴	(3.11 ± 0.37) × 10 ⁴	234 ± 25
	7_2	SS316L	—	(1.43 ± 0.27) × 10 ⁵	(4.23 ± 0.42) × 10 ³	520 ± 100	210 ± 22	(8.27 ± 0.83) × 10 ³	(2.21 ± 0.23) × 10 ⁴	173 ± 17
	21_1	Alloy 660 (IWS)	—	(1.40 ± 0.34) × 10 ⁵	(3.49 ± 0.35) × 10 ³	360 ± 102	215 ± 23	(1.10 ± 0.11) × 10 ⁴	(4.56 ± 0.47) × 10 ⁴	287 ± 29

(Continued.)

Table 2. (Continued.)

Lab	Sample Pos. ID	Material	Radionuclide Activity (Bq g^{-1})							
			^{46}Sc	^{51}Cr	^{54}Mn	^{59}Fe	^{56}Co	^{57}Co	^{58}Co	^{60}Co
IPPLM	1_4	SS316L(N)-IG	—	—	$(5.33 \pm 0.23) \times 10^3$	—	—	$(9.80 \pm 0.36) \times 10^3$	$(2.66 \pm 0.07) \times 10^4$	211 ± 6
	2_1	SS316L(N)-IG	—	—	$(5.42 \pm 0.23) \times 10^3$	—	469 ± 37	$(1.02 \pm 0.04) \times 10^4$	$(2.75 \pm 0.07) \times 10^4$	190 ± 6
	4_1	SS316L(N)	—	$(2.04 \pm 0.15) \times 10^5$	$(5.32 \pm 0.23) \times 10^3$	446 ± 32	—	$(1.02 \pm 0.04) \times 10^4$	$(2.69 \pm 0.06) \times 10^4$	184 ± 6
	8_4	SS316L(N)	—	$(2.13 \pm 0.24) \times 10^5$	$(4.58 \pm 0.20) \times 10^3$	410 ± 48	—	$(9.48 \pm 0.36) \times 10^3$	$(2.69 \pm 0.07) \times 10^4$	196 ± 6
	17_3	Tungsten	—	—	0.35 ± 0.03	—	—	0.85 ± 0.07	—	1.08 ± 0.03
	19_1	Al-Bronze	—	—	438 ± 19	—	—	$(3.75 \pm 0.16) \times 10^3$	$(1.07 \pm 0.03) \times 10^4$	734 ± 22
	4_2	Al-Bronze	—	—	447 ± 19	—	—	$(3.65 \pm 0.16) \times 10^3$	$(1.08 \pm 0.03) \times 10^4$	745 ± 23
	5_2	SS304 (IWS)	—	$(1.90 \pm 0.17) \times 10^5$	$(4.18 \pm 0.18) \times 10^3$	440 ± 39	—	$(1.01 \pm 0.04) \times 10^4$	$(2.76 \pm 0.07) \times 10^4$	199 ± 6

Table 3. Second summary table of the gamma spectrometry results from all laboratories. Measured specific activities for the radionuclides listed have been decay corrected to 21/12/2021 21:53 (the end of the DTE2 campaign) with $k = 2$ expanded uncertainties reported. Sample Pos. ID refers to the foil location within the LTIS in the form *channel_depth*, i.e. sample position ID 1_3 represents the third position in channel 1.

Lab	Sample Pos. ID	Material	Radionuclide Activity (Bq g ⁻¹)														
			⁶⁵ Zn	⁹⁵ Zr	⁹⁵ Nb	^{110m} Ag	¹⁸² Ta	¹⁸¹ Hf	¹⁸¹ W	¹⁸⁵ W							
UKAEA	1_1	SS316L(N)-IG	49.77 ± 2.32	—	491 ± 50	—	—	—	—	—	—	—	—	—	—	—	
	14_4	SS316L(N)-IG	52.15 ± 2.42	—	637 ± 64	—	—	—	—	—	—	—	—	—	—	—	
	15_4	SS316L(N)-IG	46.50 ± 2.10	—	597 ± 47	—	—	—	—	—	—	—	—	—	—	—	
	16_4	SS316L(N)	47.27 ± 2.28	—	566 ± 74	—	—	—	—	—	—	—	—	—	—	—	
	5_1	SS316L(N)	51.79 ± 2.47	—	616 ± 67	—	—	—	—	—	—	—	—	—	—	—	
	1_3	Alloy 660 (Divertor)	38.83 ± 2.01	—	—	—	—	—	—	—	—	—	—	—	—	—	—
	3_3	CuCrZr	24.60 ± 1.16	—	514 ± 37	3.44 ± 0.18	22.31 ± 0.64	—	—	—	—	—	—	—	—	—	
	4_3	CuCrZr	20.28 ± 0.99	21.76 ± 2.17	680 ± 47	1.88 ± 0.14	—	—	—	—	—	—	—	—	—	—	
	5_3	Tungsten	13.52 ± 0.61	—	—	—	140 ± 2	—	—	56.18 ± 3.20	—	—	—	—	—	(2.08 ± 0.21) × 10 ⁵	
	7_3	XM-19	43.64 ± 1.96	—	556 ± 42	—	73.23 ± 1.41	—	—	—	—	—	—	—	—	—	
	8_3	XM-19	42.05 ± 1.89	—	528 ± 42	—	70.62 ± 1.37	—	—	—	—	—	—	—	—	—	
	21_3	Inconel-718	58.11 ± 2.59	—	848 ± 57	—	532 ± 8	—	—	—	—	—	—	—	—	—	
	1_2	Eurofer 97-2	55.01 ± 2.46	—	—	—	(1.09 ± 0.02) × 10 ³	—	—	—	—	—	—	—	—	303 ± 43	
	2_2	Eurofer 97-2	46.87 ± 2.14	—	—	—	(5.26 ± 0.07) × 10 ³	—	—	—	—	—	—	—	—	—	
	3_2	Al-Bronze	44.19 ± 2.01	—	—	—	—	—	—	—	—	—	—	—	—	—	
	20_1	SS304 (IWS)	53.07 ± 2.39	—	—	—	—	—	—	—	—	—	—	—	—	—	
8_2	Alloy 660 (IWS)	37.51 ± 1.70	—	345 ± 36	—	—	—	—	—	—	—	—	—	—	—		
NCSR	13_4	SS316L(N)-IG	17.51 ± 1.53	—	—	—	—	—	—	—	—	—	—	—	—	—	
	2_4	SS316L(N)-IG	46.15 ± 3.08	—	—	—	—	—	—	—	—	—	—	—	—	—	
	3_4	SS316L(N)-IG	39.69 ± 2.86	—	—	—	—	—	—	—	—	—	—	—	—	—	
	4_4	SS316L(N)	43.63 ± 3.02	—	—	—	—	—	—	—	—	—	—	—	—	—	
	17_4	SS316L(N)	54.00 ± 3.64	—	—	—	—	—	—	—	—	—	—	—	—	—	
	18_4	SS316L(N)	36.53 ± 3.11	—	—	—	—	—	—	—	—	—	—	—	—	—	
	13_3	Alloy 660 (Divertor)	34.65 ± 3.01	—	—	—	—	—	—	—	—	—	—	—	—	—	
	2_3	Alloy 660 (Divertor)	28.26 ± 2.62	—	—	—	—	—	—	—	—	—	—	—	—	—	
	8_1	Tungsten	12.46 ± 1.24	—	—	—	—	—	—	—	—	—	—	—	—	—	
	18_3	Tungsten	11.94 ± 0.97	—	—	—	—	—	—	—	—	—	—	—	—	—	
	19_3	XM-19	33.85 ± 2.19	—	—	—	—	—	—	—	—	—	—	—	—	—	
	17_1	Inconel-718	43.45 ± 3.03	—	—	—	—	—	—	—	—	—	—	—	—	—	
	13_2	Eurofer 97-2	42.78 ± 3.37	—	—	—	—	—	—	—	—	—	—	—	—	—	
	17_2	SS304 (IWS)	40.65 ± 2.57	—	—	—	—	—	—	—	—	—	—	—	—	—	
	18_2	SS304 (IWS)	42.31 ± 2.97	—	—	—	—	—	—	—	—	—	—	—	—	—	
	19_2	SS316L	41.62 ± 3.04	—	—	—	—	—	—	—	—	—	—	—	—	—	
21_2	SS316L	46.83 ± 2.91	—	—	—	—	—	—	—	—	—	—	—	—	—		

(Continued.)

Table 3. (Continued.)

Lab	Sample Pos. ID	Material	Radionuclide Activity (Bq g ⁻¹)											
			⁶⁵ Zn	⁹⁵ Zr	⁹⁵ Nb	^{110m} Ag	¹⁸² Ta	¹⁸¹ Hf	¹⁸¹ W	¹⁸⁵ W				
ENEA	3_1	SS316L(N)-IG	—	—	—	—	—	—	—	—	—	—	—	—
	6_1	SS316L(N)	—	—	—	—	—	—	—	—	—	—	—	—
	7_4	SS316L(N)	—	—	—	—	—	—	—	—	—	—	—	—
	20_4	SS316L(N)	—	—	—	—	—	—	—	—	—	—	—	—
	9_4	SS316L(N)	—	—	—	—	—	—	—	—	—	—	—	—
	14_3	Alloy 660 (Divertor)	—	—	—	—	—	—	—	—	—	—	—	—
	9_1	XM-19	—	—	—	—	—	—	—	—	—	—	—	—
	20_3	XM-19	—	—	—	—	—	—	—	—	—	—	—	—
	9_3	Inconel-718	—	—	—	—	—	—	—	—	—	—	—	—
	15_2	Al-Bronze	—	—	—	—	—	—	—	—	—	—	—	—
	16_2	Al-Bronze	—	—	—	—	—	—	—	—	—	—	—	—
	6_2	SS304 (IWS)	—	—	—	—	—	—	—	—	—	—	—	—
	20_2	Alloy 660 (IWS)	—	—	—	—	—	—	—	—	—	—	—	—
	9_2	SS316L	—	—	—	—	—	—	—	—	—	—	—	—
15_3	CuCrZr	—	—	—	—	—	—	—	—	—	—	—	—	
16_3	CuCrZr	—	—	—	—	—	—	—	—	—	—	—	—	
14_2	Eurofer-97-2	—	—	—	—	—	—	—	(5.20 ± 0.07) × 10 ³	—	—	—	—	
IFJ-PAN	5_4	SS316L(N)	37.60 ± 3.91	—	940 ± 353	—	—	—	—	—	—	—	—	—
	6_4	SS316L(N)	45.00 ± 5.18	—	—	—	—	—	—	—	—	—	—	—
	19_4	SS316L(N)	35.10 ± 3.62	—	820 ± 266	—	—	—	—	—	—	—	—	—
	21_4	SS316L(N)	32.60 ± 3.36	—	800 ± 297	—	—	—	—	—	—	—	—	—
	7_1	CuCrZr	—	—	(1.96 ± 0.55) × 10 ³	4.80 ± 2.11	19.10 ± 9.42	—	—	—	—	—	—	—
	6_3	Tungsten	11.80 ± 1.36	—	310 ± 156	—	122 ± 14	—	—	(7.93 ± 0.96) × 10 ⁴	—	—	—	—
	18_1	Eurofer-97-2	56.40 ± 6.37	—	—	—	—	—	—	—	—	—	—	—
	7_2	SS316L	39.60 ± 4.04	—	840 ± 341	—	—	—	—	11.00 ± 3.74	—	—	—	—
	21_1	Alloy 660 (IWS)	26.80 ± 2.87	—	—	—	—	—	—	11.40 ± 7.10	—	—	—	—
	IPPLM	1_4	SS316L(N)-IG	43.76 ± 2.22	—	—	—	—	—	—	—	—	—	—
2_1		SS316L(N)-IG	45.01 ± 2.21	—	—	—	—	—	—	—	—	—	—	—
4_1		SS316L(N)	42.68 ± 1.97	—	504 ± 92	—	—	—	—	—	—	—	—	—
8_4		SS316L(N)	43.03 ± 2.18	—	—	—	—	—	—	—	—	—	—	—
17_3		Tungsten	13.21 ± 0.58	—	—	—	—	—	—	23.81 ± 2.70	—	—	—	—
19_1		Al-Bronze	39.95 ± 2.58	—	—	—	—	—	—	121 ± 2	—	—	—	—
4_2		Al-Bronze	40.50 ± 2.59	—	—	—	—	—	—	—	56.27 ± 4.00	—	—	(2.07 ± 0.14) × 10 ⁵
5_2		SS304 (IWS)	43.80 ± 2.12	—	—	—	—	—	—	—	—	—	—	—

allowing for improved identification and quantification of some radionuclides.

For instance, by comparing the CSS and non-CSS spectra in figure 5(b) (red and black lines, respectively), the two ^{95}Zr peaks at 724.2 keV and 756.7 keV (highlighted in green) are notably distinct within the CSS measurement. Furthermore, ^{95}Nb , ^{58}Co , and ^{54}Mn peaks exhibit significantly enhanced signal-to-background ratios, particularly in the energy range of approximately 750–850 keV. However, for $^{110\text{m}}\text{Ag}$ emission at 657.5 keV, the CSS spectra do not exhibit a pronounced photopeak, unlike the weak representation in the non-CSS spectra. This phenomenon indicates that, for complex and rapid coincident emission decay schemes such as $^{110\text{m}}\text{Ag}$, some characteristic gamma emissions used for identification can be vetoed by the CSS. Nevertheless, the availability of both CSS and non-CSS spectra is valuable as analysis options for complex samples containing multiple radionuclides.

5. Simulation method to predict sample specific activities

Comprehensive neutron activation calculations were conducted for every sample located within the LTIS. These calculations predict the time-dependent evolution of radionuclide generation during irradiation within JET's experimental campaigns, accounting for transmutation and subsequent radioactive decay. This assessment employed a detailed JET radiation transport model with the FISPACT-II inventory code [28]. The ITER material elemental compositions used in the simulations were based on the information in the materials certificates provided to F4E from manufacturers. The calculations incorporated experimental determinations of neutron yield (and spectral) fluctuations during JET experiments.

A JET radiation transport model was developed for use with the MCNPv6.2 [35] code and the FENDL-3.1b [36] radiation transport library. This model was used to calculate neutron spectra and relevant nuclear reaction rates averaged over specific material cell volumes within the LTIS for three distinct plasma neutron source modes: D–D, T–T, and D–T. The MCNP model encompassed a detailed representation of the LTIS and ACT sub-holder, accurately reflecting the sample loading configuration depicted in figure 2. Separate simulations were conducted for each plasma neutron source mode using the coupled neutron-gamma mode. The Automated VARIance reducTION Generator (ADVANTG) software [37] was employed to generate an optimised weight window map, subsequently applied to the production calculation to reduce variance in neutron flux tally at the LTIS position. All results from volumetric neutron flux (F4 tally) surpassed the 10 statistical tests, confirming satisfactory convergence of the simulations.

For FISPACT-II inventory calculations, the outputs from the MCNP simulations were coupled with relevant measured neutron yield data corresponding to D–D, T–T, and D–T plasma components during the experimental periods. To accurately model neutron capture reactions, particularly those involving self-shielding effects, MCNP-derived pointwise

spectrum averaged cross sections were incorporated into FISPACT-II calculations for dosimetry reaction channels in IRDFF-II [38]. For reaction channels not present in IRDFF-II, data were taken from the JEFF 3.3 pointwise library, where available. For all other reaction channels not covered by these two libraries and for the volume-averaged neutron spectrum calculated within the sample using MCNP, the TENDL-2017 group-wise activation library in 709 energy groups was applied.

The input data for inventory simulations was derived from total neutron yield measurements that characterised the irradiation history. The LTIS, containing the samples, was installed on the 4th October 2020 (with the first JET shot after installation on the 8th October 2020, designated as shot 98020). The final neutron exposure before the LTIS retrieval occurred on the 23rd September 2022 (shot 101175, with the retrieval operation on the 25th September). During its 715-day installation in JET, comprising 3155 experimental shots, the total neutron yield reached 8.67×10^{20} neutrons. This neutron yield was measured using the KN1 fission chamber diagnostic system, composed of pairs of ^{235}U and ^{238}U -based fission chambers. Additional details on this diagnostic system can be found in [3, 39]. The contributions to the neutron yield from D–T, T–T, and D–D components were measured as 8.51×10^{20} , 7.07×10^{18} , and 8.96×10^{18} , respectively, during this period (verified through summation of the neutron yield data per shot over the installed period of the LTIS using data formally released on 6th July 2023 [40]).

The temporal profile of neutron fluence was modeled using FISPACT-II with a 1-day time resolution employing flat-top pulses. These pulses were calculated by multiplying the KN1 daily neutron yield with the appropriate MCNP flux normalization for the respective sample position within the LTIS and considering the corresponding D–T, T–T, and D–D neutron spectrum components. Subsequently, this temporal irradiation history data served as input for FISPACT-II calculations, conducted separately for the three neutron spectrum components and then summed to yield total activities for each radionuclide.

5.1. Simulation results

Figure 6 (bottom plot) displays the variation in JET's daily neutron fluence ϕ_T for D–D, D–T, and T–T neutron spectrum components, averaged over the LTIS sample location. The red dashed vertical line denotes the time of tritium introduction during the experimental campaign. The black dashed vertical line indicates when the LTIS was removed from JET. The top plots show the predicted specific activity results over time for various dominant radionuclides obtained from these activation calculations for a tungsten divertor monoblock sample and a CuCrZr sample, respectively (the corresponding gamma spectra for these samples are shown earlier in this paper in figure 5). The D–T, T–T and D–D neutron fluence per unit lethargy, ϕ_L , energy spectrum per plasma source neutron averaged over the sample volume are shown as inset plots. With the LTIS sample positions being close to the vacuum vessel, there is only a small amount of shielding between the plasma

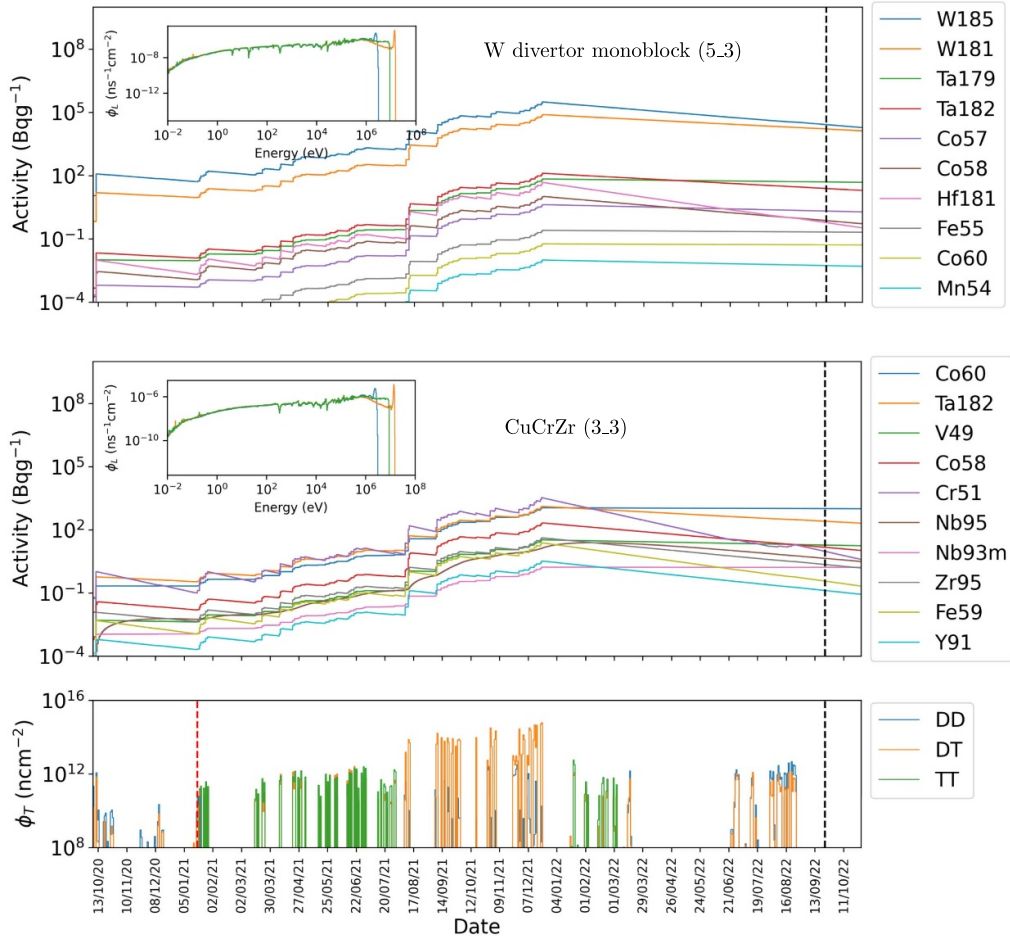


Figure 6. Temporal specific activity predictions of dominant radionuclides during and following JET irradiation of a W monoblock sample (top plot, position reference 5_3) and a CuCrZr sample (middle plot, position reference 3_3). The black dashed vertical line denotes when the LTIS containing the samples was removed from the JET LTIS. The LTIS was installed into JET on the 4th October 2020. The inset plots show the neutron fluence per unit lethargy, ϕ_L , energy spectrum averaged over the sample volume within the LTIS, calculated using MCNP. Bottom plot: daily neutron fluence averaged over the sample volume within the LTIS, ϕ_T for D–D, D–T and T–T spectrum components. The red dashed vertical line denotes the introduction of tritium within the experimental campaign.

and the samples, allowing for a relatively high fraction of unscattered 14 MeV neutrons incident on the samples, as evidenced by the 14 MeV peak that is evident in the D–T spectra in the plot insets. For reference, the average D–T neutron fluence for example material samples: CuCrZr, Tungsten, and Eurofer 97-2 were $4.97 \times 10^{15} \text{ n cm}^{-2}$, $4.93 \times 10^{15} \text{ n cm}^{-2}$ and $4.89 \times 10^{15} \text{ n cm}^{-2}$, respectively.

5.2. Validation of simulations using dosimetry foil-based diagnostics

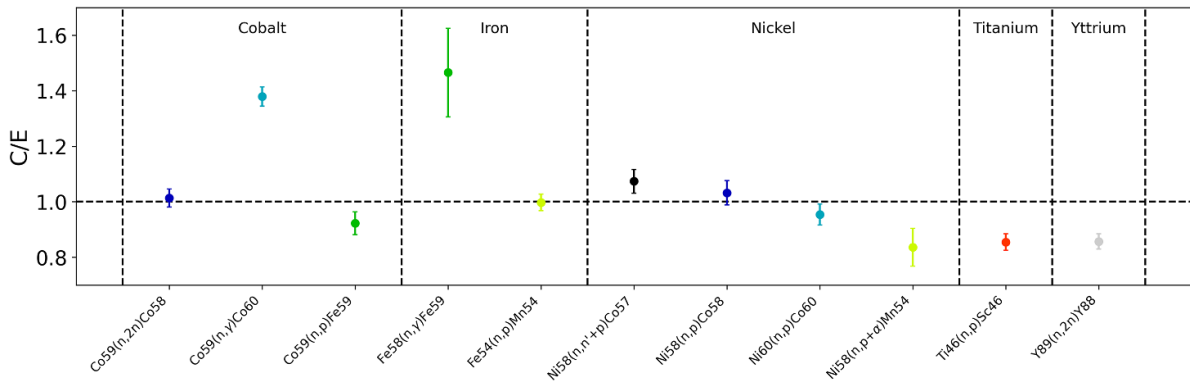
A range of high-purity dosimetry foil-based diagnostics, including Co, Fe, Ni, Ti and Y foils, were also loaded into the LTIS for use as diagnostics. Similar to the analysis approach described in earlier sections for measurement of the ITER samples, the dosimetry foils were measured post-irradiation using gamma spectrometry techniques to identify key reaction products associated with the nuclear reactions in table 4 and to quantify their activity. Calculated predictions (C) were compared against experimentally measured data (E) to produce

C/E results. The C/E values per reaction are shown in figure 7 as a weighted average per reaction (each measurement was weighted by its inverse variance).

For the dosimetry foil measurements, some general comments can be made relating to the threshold reactions, which are sensitive to the fast neutron spectrum above a few MeV (see the threshold energies in table 4), and the capture reactions, which are significantly more sensitive to low energy neutrons through their characteristic cross section which is proportional to $1/v$ at low energy. The reactions in figure 7 include two capture reactions, $^{59}\text{Co}(n,\gamma)^{60}\text{Co}$ and $^{58}\text{Fe}(n,\gamma)^{59}\text{Fe}$, and nine threshold reactions. The weighted average C/E across all dosimetry measurements is 0.986 ± 0.007 . The nine threshold reaction calculations yielded an overall weighted average C/E of 0.941 ± 0.008 . The weighted average for the two capture reaction measurements is 1.38 ± 0.02 , indicating that the JET MCNP model result may be overestimating the thermal neutron flux in the LTIS location. Alternative possibilities are that self-shielding from adjacent materials to the LTIS, unaccounted for in the model, are

Table 4. Dosimetry foil types, associated reactions and their principle gamma emission lines. 50% energy threshold ($E_{\text{thr}50}$) were derived from IRDF data [38].

Foil material	Reaction; (dominant pathway)	Principle gamma line(s) (keV) [41]	$E_{\text{thr}50}$
Co	$^{59}\text{Co}(n,2n)^{58}\text{Co}$	810.759	12.7 MeV
	$^{59}\text{Co}(n,\gamma)^{60}\text{Co}$	1173.228, 1332.492	—
Fe	$^{58}\text{Fe}(n,\gamma)^{59}\text{Fe}$	1099.245, 1291.590	—
	$^{\text{nat}}\text{Fe}(n,x)^{54}\text{Mn}$; ($^{54}\text{Fe}(n,p)^{54}\text{Mn}$)	834.838	3.7 MeV
	$^{\text{nat}}\text{Ni}(n,x)^{58}\text{Co}$; ($^{58}\text{Ni}(n,p)^{58}\text{Co}$)	810.759	3.7 MeV
Ni	$^{\text{nat}}\text{Ni}(n,x)^{60}\text{Co}$; ($^{60}\text{Ni}(n,p)^{60}\text{Co}$)	1173.228, 1332.492	8.3 MeV
	$^{\text{nat}}\text{Ni}(n,x)^{57}\text{Co}$; ($^{58}\text{Ni}(n,n'p)^{57}\text{Co}$)	14.413, 122.061, 136.474	12.8 MeV
Ti	$^{\text{nat}}\text{Ti}(n,x)^{46}\text{Sc}$; ($^{46}\text{Ti}(n,p)^{46}\text{Sc}$)	889.271, 1120.537	6.3 MeV
Y	$^{89}\text{Y}(n,2n)^{88}\text{Y}$	898.036, 1836.052	13.3 MeV

**Figure 7.** C/E values for sets of dosimetry foil reactions. Standard experimental uncertainties are reported at $k = 1$.

not fully captured, or a combination of both thermal flux overestimation and self-shielding factors are responsible for this deviation. The slightly low C/E for threshold reactions may indicate that the model slightly underestimated the high-energy neutron fluence. However, it should be recognised that the current result is within the uncertainty bounds associated with the KN1 neutron yield instrument, which feeds into the calculation part of this assessment, quoted as 10%.

6. Discussion: comparison of experimental against calculation results

C/E values were calculated for the set of the ITER materials, as shown in figure 8. These present in (a) the C/E values per measured isotope with measurement laboratories identified, (b) the same C/E data set but grouped by the material type, and (c) the weighted average C/E values grouped by material type. The weighted average C/E values of isotope measurements for ^{46}Sc , ^{51}Cr , ^{54}Mn , ^{59}Fe , ^{57}Co , ^{95}Nb , and ^{181}Hf are in general closest to 1 when excluding materials with outliers, as shown in table 5. ^{58}Co , ^{60}Co , and ^{181}W were not included in this list despite their overall weighted averages being within 0.75–1.25 since the individual material weighted averages (shown in table 6) are not, in general, close to 1.

It is important to emphasise that due to the composition of these materials, consisting of many elements (unlike the high

elemental purity dosimetry foil materials), in some cases the reaction product isotope could be generated through multiple distinct reaction pathways leading to the formation of the same isotope. For instance, the data for ^{60}Co can involve reaction pathways arising from both $^{59}\text{Co}(n,\gamma)^{60}\text{Co}$ and $^{60}\text{Ni}(n,p)^{60}\text{Co}$ reactions in cases where both Ni and Co are present in the material.

Exceptions were identified in measurements for ^{54}Mn in CuCrZr (reference 3_3 and 7_1) and W monoblock samples (reference 5_3, 6_3 and 17_3), which exhibited low C/E values. Dominant reaction pathways for ^{54}Mn production were from Fe seed nuclides such as $^{56}\text{Fe}(n,t)^{54}\text{Mn}$ or $^{54}\text{Fe}(n,p)^{54}\text{Mn}$. The CuCrZr material certificates do not list Fe as an impurity. Although ^{54}Mn is generated in very small quantities through multiple reactions from Co or Cu, the observed activity was much higher than would be predicted from these pathways (the ^{54}Mn activity was predicted through FISPACT-II to be of the order $1 \times 10^{-10} \text{ Bq g}^{-1}$, which would be significantly below the gamma spectrometry measurement detection limit). The measured ^{54}Mn activities in the CuCrZr samples of $(1.24 \pm 0.13) \text{ Bq g}^{-1}$ and $(1.64 \pm 0.54) \text{ Bq g}^{-1}$ were small compared to some other materials, though were much higher than expected (hence why the C/E values are very low). It is probable that the CuCrZr samples contained a Fe impurity not accounted for in the material certificate. Future work in material composition analysis will aim to investigate this. The W monoblock material certificate listed Fe as a 2 ppm impurity, so the C/E values

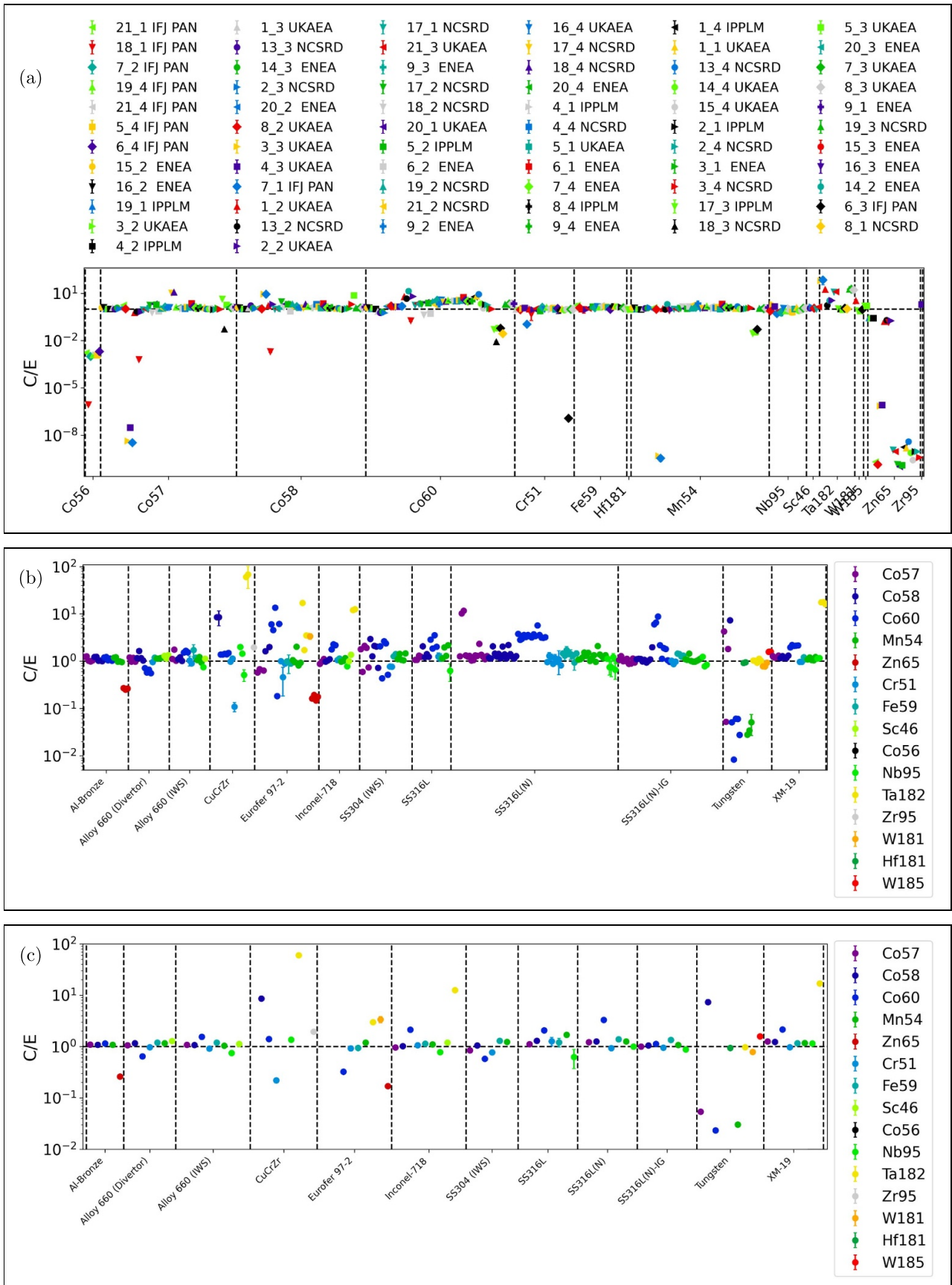


Figure 8. C/E values for measured and calculated ITER materials: (a) all results grouped by measured isotope. The legend indicates the position–depth ID; (b) all results grouped by material type. (c) Weighted average results by material type.

Table 5. Weighted average C/E values per radionuclide, associated uncertainty and range for all ITER samples. Where stated, for some radionuclides, some materials have been excluded from the weighted average calculations and presented in a separate row using a material weight average; this prevents outliers from dominating the weighted average of all materials.

Radionuclide	C/E and uncertainty	Minimum C/E value	Maximum C/E value
⁴⁶ Sc	1.21 ± 0.02	1.00	1.38
⁵¹ Cr (excl. Tungsten)	0.93 ± 0.02	0.46 (Eurofer 97-2)	1.30
⁵¹ Cr (Tungsten)	(1.17 ± 0.27) × 10 ⁻⁷	1.17 × 10 ⁻⁷	1.17 × 10 ⁻⁷
⁵⁴ Mn (excl. CuCrZr, Tungsten)	1.150 ± 0.007	0.82	2.18
⁵⁴ Mn (CuCrZr)	(4.49 ± 0.46) × 10 ⁻¹⁰	3.38 × 10 ⁻¹⁰	4.71 × 10 ⁻¹⁰
⁵⁴ Mn (Tungsten)	0.030 ± 0.002	0.028	0.051
⁵⁹ Fe	1.17 ± 0.01	0.89	1.73
⁵⁶ Co (excl. Eurofer 97-2)	(1.24 ± 0.06) × 10 ⁻³	9.60 × 10 ⁻⁴ (SS316L)	2.01 × 10 ⁻³ (SS316L(N))
⁵⁶ Co (Eurofer 97-2)	(8.84 ± 1.21) × 10 ⁻⁷	8.8 × 10 ⁻⁷	8.8 × 10 ⁻⁷
⁵⁷ Co (excl. CuCrZr, Eurofer 97-2)	1.051 ± 0.007	0.599 (SS304 (IWS))	4.296 (Tungsten)
⁵⁷ Co (CuCrZr)	(4.33 ± 0.29) × 10 ⁻⁹	3.35 × 10 ⁻⁹	3.07 × 10 ⁻⁸
⁵⁷ Co (Eurofer 97-2)	(6.41 ± 0.69) × 10 ⁻⁴	6.37 × 10 ⁻⁴	0.68
⁵⁸ Co (excl. Eurofer 97-2)	1.107 ± 0.005	0.64 (SS304 (IWS))	8.58 (CuCrZr)
⁵⁸ Co (Eurofer 97-2)	(2.01 ± 0.24) × 10 ⁻³	2.00 × 10 ⁻³	2.00
⁶⁰ Co (excl. Tungsten)	1.006 ± 0.004	0.18 (Eurofer 97-2)	13.54 (Eurofer 97-2)
⁶⁰ Co (Tungsten)	(2.34 ± 0.06) × 10 ⁻²	8.31 × 10 ⁻³	6.10 × 10 ⁻²
⁶⁵ Zn (only Al-Bronze, Eurofer 97-2)	0.192 ± 0.004	0.15 (Eurofer 97-2)	0.27 (Al-Bronze)
⁶⁵ Zn (other materials)	(4.32 ± 0.09) × 10 ⁻¹⁰	1.02 × 10 ⁻¹⁰ (SS304 (IWS))	8.26 × 10 ⁻⁷ (CuCrZr)
⁹⁵ Zr (CuCrZr)	1.95 ± 0.20	1.95	1.95
⁹⁵ Zr	<MDA	—	—
⁹⁵ Nb	0.95 ± 0.02	0.51 (CuCrZr)	2.00 (CuCrZr)
^{110m} Ag	0	—	—
¹⁸² Ta (only CuCrZr, Inconel-718, XM-19)	14.52 ± 0.14	12.13 (Inconel-718)	68.38 (CuCrZr)
¹⁸² Ta (only Eurofer 97-2 and Tungsten)	1.210 ± 0.009	0.92 (Tungsten)	17.13 (Eurofer 97-2)
¹⁸¹ Hf	0.94 ± 0.04	0.92 (Tungsten)	0.95 (Tungsten)
¹⁸¹ W	0.79 ± 0.03	0.77 (Tungsten)	3.37 (Eurofer 97-2)
¹⁸⁵ W	1.58 ± 0.09	1.58 (Tungsten)	1.60 (Tungsten)

are not as low as CuCrZr, but small deviations in composition will have a large effect on the C/E value.

For ⁵¹Cr, low C/E were seen with values of (1.2 ± 0.3) × 10⁻⁷ in one W monoblock sample (reference 6_3) and 0.11 ± 0.02 in a CuCrZr sample (reference 7_1), which were omitted from the overall weighted average in table 5. In the case of the W monoblock, Cr was not listed as an impurity in the material certificate. If Cr were present this may explain the observed C/E value, with ⁵¹Cr being generated through the ⁵²Cr(n,2n)⁵¹Cr and, to a lesser extent, the ⁵⁴Fe(n,α)⁵¹Cr reaction. In the case of the low C/E value observed for ⁵¹Cr in the CuCrZr samples, it is noted that the CuCrZr material certificate gives a Cr component of 0.6% to 0.9%. Even though FISPACT-II calculations presented in this report used the conservative approach of using the maximum concentration in the material definition, the low C/E seen may indicate that the true Cr content is higher than is stated in the certificate.

The nuclide results with high C/E were ⁵⁸Co, ⁶⁰Co, ⁹⁵Zr, ¹⁸²Ta, and ¹⁸⁵W. A relatively greater spread was evident for ⁶⁰Co. Most of the 68 data points (⁶⁰Co was measured in all of the ITER samples) presented tended to have values above 1, apart from 13 data points. The variation is thought to arise from the several possible competing reaction pathways for ⁶⁰Co, including ⁵⁹Co(n,γ)⁶⁰Co, ⁶⁰Ni(n,p)⁶⁰Co, ⁶¹Ni(n,d)⁶⁰Co, and ⁶³Cu(n,α)⁶⁰Co. Differences in the abundance of these

seed nuclides in a sample from the material certificate will lead to differences in the predicted activity compared to measurements and deviations in the C/E value from 1. Of the 12 material types that ⁶⁰Co was measured, only two are within 25% of 1, with six materials exhibiting a C/E weighted average > 1.25 and four materials producing a C/E weighted average < 0.75. The largest variation observed was in Eurofer 97-2, which had both the minimum and maximum C/E values across the range of materials (excluding the anomalously low C/E in W monoblock). This is attributed to the small and comparable Ni, Co and Cu components in the material certificate, each with a maximum of 0.01%, as localised composition fluctuation in the Eurofer 97-2 samples would give significantly different results. The anomalously low W monoblock C/E shows further evidence that the impurities have not been fully captured in the material certificate as the C/E of other typical steel activation products indicate.

High C/E values for ¹⁸²Ta measurements were observed in several ITER material samples, namely CuCrZr, Inconel-718 and XM-19. CuCrZr had particularly high C/E values with a material weighted average of 60.3 ± 0.017 and a highest value of 68.4, the highest C/E value found in the entire dataset. Comparatively, Eurofer 97-2 has a ¹⁸²Ta weighted average C/E much closer to 1 despite one sample having a C/E of 17.1, whereas the W monoblock samples all have a ¹⁸²Ta

Table 6. Weighted average C/E values per radionuclide, associated uncertainty and range for each material type in the ITER samples.

Radionuclide	Material											
	Al-Bronze	Alloy 660 (Divertor)	Alloy 660 (IWS)	CuCrZr	Eurofer 97-2	Inconel-718	SS304 (IWS)	SS316L	SS316L(N)	SS316L(N)-IG	Tungsten	XM-19
⁴⁶ Sc	—	1.28 ± 0.03	1.13 ± 0.04	—	—	1.19 ± 0.06	—	—	—	—	—	—
⁵¹ Cr	—	0.96 ± 0.08	0.91 ± 0.07	0.22 ± 0.02	0.92 ± 0.05	1.06 ± 0.09	0.77 ± 0.05	1.26 ± 0.23	0.94 ± 0.04	0.95 ± 0.04	(1.17 ± 0.27) × 10 ⁻⁷	0.97 ± 0.05
⁵⁴ Mn	1.08 ± 0.02	1.11 ± 0.02	1.04 ± 0.03	(4.49 ± 0.46) × 10 ⁻¹⁰	1.19 ± 0.03	1.10 ± 0.03	1.19 ± 0.02	1.56 ± 0.04	1.23 ± 0.01	1.05 ± 0.02	0.030 ± 0.002	1.17 ± 0.02
⁵⁹ Fe	—	1.20 ± 0.07	1.20 ± 0.05	—	0.94 ± 0.03	1.14 ± 0.04	1.29 ± 0.05	1.21 ± 0.23	1.38 ± 0.04	1.35 ± 0.03	—	1.16 ± 0.03
⁵⁶ Co	—	—	(1.73 ± 0.18) × 10 ⁻³	—	(8.84 ± 1.21) × 10 ⁻⁷	—	—	(9.60 ± 0.99) × 10 ⁻⁴	(1.33 ± 0.08) × 10 ⁻³	—	—	—
⁵⁷ Co	1.09 ± 0.02	1.06 ± 0.02	1.08 ± 0.03	(4.33 ± 0.29) × 10 ⁻⁹	(6.41 ± 0.69) × 10 ⁻⁴	0.97 ± 0.03	0.85 ± 0.02	1.12 ± 0.03	1.17 ± 0.01	1.00 ± 0.02	2.13 ± 0.14	1.25 ± 0.03
⁵⁸ Co	1.09 ± 0.01	1.12 ± 0.02	1.07 ± 0.02	8.56 ± 0.62	(2.01 ± 0.24) × 10 ⁻³	1.05 ± 0.02	0.96 ± 0.02	1.22 ± 0.03	1.23 ± 0.01	1.03 ± 0.01	7.34 ± 0.80	1.23 ± 0.02
⁶⁰ Co	1.15 ± 0.01	0.643 ± 0.009	1.54 ± 0.03	1.40 ± 0.02	0.33 ± 0.02	2.12 ± 0.03	0.577 ± 0.009	2.09 ± 0.04	3.29 ± 0.03	1.127 ± 0.009	0.0234 ± 0.0006	2.15 ± 0.03
⁶⁵ Zn	0.259 ± 0.008	—	(1.41 ± 0.06) × 10 ⁻¹⁰	(7.42 ± 0.25) × 10 ⁻⁷	0.170 ± 0.005	(9.74 ± 0.37) × 10 ⁻¹⁰	(1.12 ± 0.03) × 10 ⁻¹⁰	—	—	(3.96 ± 0.10) × 10 ⁻¹⁰	—	—
⁹⁵ Zr	—	—	—	1.95 ± 0.20	—	—	—	—	—	—	—	—
⁹⁵ Nb	—	—	0.75 ± 0.08	1.36 ± 0.07	—	0.78 ± 0.05	—	0.63 ± 0.25	0.99 ± 0.07	0.88 ± 0.05	—	1.15 ± 0.06
^{110m} Ag	—	—	—	0	—	—	—	—	—	—	—	—
¹⁸² Ta	—	—	—	60.32 ± 1.73	2.95 ± 0.03	12.60 ± 0.17	—	—	—	—	—	0.97 ± 0.01
¹⁸¹ Hf	—	—	—	—	—	—	—	—	—	—	—	0.94 ± 0.04
¹⁸¹ W	—	—	—	—	3.37 ± 0.48	—	—	—	—	—	—	0.78 ± 0.03
¹⁸⁵ W	—	—	—	—	—	—	—	—	—	—	—	1.58 ± 0.09

C/E close to 1, with them all within 13%. The trend in these ^{182}Ta C/E values follows which production reaction pathway is available and to what extent. Under neutron irradiation, ^{182}Ta is produced from Ta in the reaction $^{181}\text{Ta}(n,\gamma)^{182}\text{Ta}$ and from W in the reaction $^{182}\text{W}(n,p)^{182}\text{Ta}$ and $^{184}\text{W}(n,t)^{182}\text{Ta}$. The best C/E values were in the materials containing W in their certificates, W monoblock and Eurofer 97-2. Poorer C/E values occurred in materials containing Ta, and the C/E values became worse in materials with Ta content but without W. W monoblock with the best ^{182}Ta C/E has a material certificate with no Ta and 99.97% W. The material certificate with both Ta (0.10% to 0.14%) and W (1.0% to 1.2%) was Eurofer 97-2, whilst the three other materials with the poorest ^{182}Ta C/E contain Ta but not W and the lower the Ta content, the further the C/E was from 1. The material certificates stated that Inconel 718 has a Ta content of 0.05% max., XM-19 has 0.01%, and CuCrZr has 0.003% to 0.01%. The reason W content produced better ^{182}Ta C/E results is explainable through higher quality nuclear data for the threshold reactions compared to the Ta capture reaction and the abundance of seed nuclide in the material that could produce ^{182}Ta . For example, all five W monoblock sample measurements identified ^{182}Ta in their spectra, while only two of the five CuCrZr identified ^{182}Ta , indicating a low activity where results are more susceptible to fluctuations. Any fluctuations in ^{182}Ta content that might highlight discrepancies in the material certificates will be investigated through additional independent element analysis later in this project. Eurofer 97-2 also exhibited a high C/E for ^{181}W , which since it was produced via the $^{182}\text{W}(n,2n)^{181}\text{W}$ reaction indicates the certificate W value is too high and would also explain the ^{182}Ta overprediction.

Only 7 out of 59 ITER samples where ^{58}Co was measured exhibited C/E values less than 1. Primary routes for the production of ^{58}Co are expected to be through $^{59}\text{Co}(n,2n)^{58}\text{Co}$ or $^{58}\text{Ni}(n,p)^{58}\text{Co}$ reactions and so variation in the elemental composition of Ni or Co, or both in the samples could be responsible. High ^{58}Co C/E values were seen in CuCrZr from two samples and W monoblock from one sample. These results indicate that the FISPACT-II calculations have overpredicted the ^{58}Co activity and suggest the certificates may have overpredicted the Co and Ni content, respectively. A reduced Co content with an increased Fe, Cr, and Ni in CuCrZr would explain the elevated ^{58}Co C/E and low C/E values for ^{54}Mn , ^{51}Cr , and ^{57}Co ; while a reduced Ni content with increased Fe and Cr would explain the elevated ^{58}Co and ^{57}Co C/E values and low ^{54}Mn and ^{51}Cr C/E values in W monoblock.

^{95}Zr was predicted in some materials, as shown in figure 9, but only observed in one gamma spectrometry measurement of a CuCrZr sample. This was because the FISPACT-II predicted activities were less than the measurement minimum detectable activities (MDA). Of the materials that expected ^{95}Zr , the predicted activity was between 14% and 70% of the MDA. ^{95}Zr might be present in the spectra but just not observable so there are no C/E values for these materials, which have been omitted from tables 5 and 6 and given as <MDA. There were low C/E values in measurements of ^{56}Co and ^{65}Zn . In addition, $^{110\text{m}}\text{Ag}$ was unexpectedly identified with activities in the range 1.9Bq g^{-1} to 4.8Bq g^{-1} in CuCrZr samples (sample

references 3_3, 4_3 and 7_1). Without a calculation (C) value to accompany with these experimental (E) values, the C/E value in the table is listed as 0.

The anomalous presence of ^{65}Zn observed in numerous samples, typically detected at low activity levels of around a few tens of Bq g^{-1} , is likely to be explained by the employed sample preparation method. This preparation method involved the widely used Electrical Discharge Machining (EDM) technique, frequently employed in manufacturing processes. In EDM, a brass wire is continually fed through the material while maintaining a small gap between the wire and the sample. Controlled material removal occurs due to electrical discharges between the wire and the workpiece.

The verification of brass (comprising Cu and Zn) on the sample surfaces was conducted using a scanning electron microscope (SEM) in conjunction with a wavelength dispersive spectrometer (WDS) to determine the material composition. Further studies are ongoing, which are expected to be reported in detail in the future. The probable origin of the ^{65}Zn can be attributed to the $^{64}\text{Zn}(n,\gamma)^{65}\text{Zn}$ reaction, which would be most sensitive to the thermal neutron flux within the LTIS. Consequently, even where ^{65}Zn was expected (Al-Bronze and Eurofer 97-2), the C/E values are significantly smaller than 1. The only other activation product of brass expected to be measurable in gamma spectrometry that might have affected the results in this report was ^{60}Co through the reaction $^{63}\text{Cu}(n,\alpha)^{60}\text{Co}$; this might partially explain the low C/E values observed in some materials and the anomalously low ^{60}Co C/E seen in tungsten. However, since several materials had ^{60}Co C/E values above 1, there are likely other causes, as explained earlier. The brass deposition highlights the significance of considering both component and material sample preparation when evaluating the complete radiological inventory during and after irradiation in fusion conditions. Notably, recently treated, unirradiated ITER samples have undergone surface polishing to attempt to eliminate trace brass. These polished samples were installed in the JET for irradiation as part of the recent DTE3 campaign, with additional post-irradiation analysis anticipated to complete in late 2024.

It may seem obvious that machining processes can introduce impurities; however, the findings in this study emphasises the need for more precise material composition data, potentially beyond what is provided in manufacturer certificates. It also extends to specific cutting and tooling methods as this study also highlights the potential for surface contamination due to machining techniques.

A key contribution of this work is the provision of quantitative activity measurements of samples, demonstrating that the accuracy of simulations is highly dependent on precise input data. While testing every material piece in the ITER machine may be impractical, further research is necessary to improve material verification and quality assurance. Although a comprehensive reactor-wide analysis is ideal, it is likely to be limited by cost constraints.

The collaboration is currently implementing independent chemical analyses, such as ICP-MS, starting with CuCrZr and W samples, with plans for broader application as budget

ITER Mat.	Material	Sc-46	Cr-51	Mn-54	Fe-59	Co-56	Co-57	Co-58	Co-60	Zn-65	Zr-95	Nb-95	Ag-110m	Ta-182	Hf-181	W-181	W-185
ITER#1	SS316L (N) -vv plate																
ITER#2	SS316L (N) - wv plate																
ITER#3	SS316L (N) - wv plate																
ITER#4	SS316L (N) - TF plate																
ITER#5	SS316L (N) - TF plate																
ITER#6	SS316L (N) - TF plate																
ITER#7	SS316L (N) - TF plate																
ITER#8	SS316L (N) - TF plate																
ITER#9	SS316L (N) - TF plate																
ITER#10	Alloy 660 – divertor																
ITER#11	Alloy 660 – divertor																
ITER#12	CuCrZr divertor pipe																
ITER#13	CuCrZr divertor pipe																
ITER#14	Tungsten																
ITER#15	Tungsten																
ITER#16	Divertor XM-19																
ITER#17	Divertor XM-19																
ITER#18	Inconel 718																
ITER#19	Eurofer 97-2																
ITER#20	Eurofer 97-2																
ITER#21	Divertor Al-Bronze																
ITER#22	Divertor Al-Bronze																
ITER#23	SS304 – In-wall shield																
ITER#24	SS304 – In-wall shield																
ITER#25	SS316 – PF Jacket																
ITER#26	Alloy 660 – IWS A286																
ITER#27	SS316 - Divertor																

Predicted and measured	
Measured, not predicted	
Predicted, not measured	
Not predicted, not measured*	

*Note that this subset of nuclides only corresponds to those measured in at least one ITER sample and that other nuclides may be predicted, but not measured in these samples. A nuclide is considered predicted if it was in the top 10 most active nuclides or its activity was >0.5 Bq/g on 28/10/2022 in FISPACT-II calculations.

Figure 9. Overview matrix of prediction and measurement results for ITER materials indicating isotopes that were: predicted and measured; measured but not predicted; predicted and not measured; and not predicted or measured. Note that the subset of radionuclides here corresponds to those measured in at least one ITER sample within the set and that other radionuclides may be predicted to be present in these samples but were not measured in this study.

permits. Future research will focus on modeling the impact of these findings on predictions of radioactive waste generation and maintenance-related shutdown dose rates, utilizing the latest ITER neutronics models.

7. Conclusions

Unique experience has been gained in characterisation and neutron activation studies for ITER materials in a tokamak environment operating with significant nuclear conditions. These experimental findings constitute the first evaluation of a diverse array of ITER materials subjected to irradiation within a tokamak-based D–T neutron environment. 68 ITER material samples were exposed to neutrons from the JET plasma, yielding 8.67×10^{20} neutrons over 715 days, spanning 3155 experimental shots. Following irradiation, these samples were retrieved and allocated to laboratories for post-irradiation examination via gamma spectrometry techniques. The analysis discerned and quantified 16 radionuclides across the comprehensive set of ITER material samples. These experimental observations were then compared against high-fidelity neutronics modeling predictions.

Dosimetry foil-based diagnostic measurements within the long-term irradiation station confirm a robust agreement between calculated neutron fluence for the fast neutron spectrum and experimental observations. The weighted average C/E across all dosimetry measurements was 0.986 ± 0.07 , weighted by the inverse variance. The subset of nine threshold reactions C/E gave an overall weighted average value of 0.941 ± 0.08 , and capture reactions returned C/E results of 1.38 ± 0.02 . The uncertainty in the KN1 neutron yield diagnostic is reported as 10%, and so the fast neutron fluence is consistent (within uncertainties) with measurement. This result may indicate a possible overestimate of the simulated thermal neutron flux within the long-term irradiation stations. This discrepancy could also originate from factors such as self-shielding effects from adjacent materials or unaccounted-for details in the model.

Regarding the ITER material results, this work presents an overview of the entire C/E dataset for each measured isotope. Generally, C/E values closest to 1 (within 25%) were observed for isotopes such as ^{46}Sc , ^{51}Cr , ^{54}Mn , ^{59}Fe , ^{95}Nb , and ^{181}Hf . However, high ^{58}Co C/E values of 7.34 and 8.56 were seen in CuCrZr and tungsten, respectively. Slightly elevated C/E values, ranging from 1.40 to 3.36 were noted for ^{60}Co , ^{95}Zr , ^{181}W , and ^{185}W in some materials. For instance, ^{60}Co exhibited six materials with weighted average C/E values > 1.25 , but also four materials with weighted averages < 1.25 with only two materials within 25% of a C/E of 1. These discrepancies compared to measurement data might stem from uncertainties in materials certificates and an overestimation of the thermal neutron flux in the MCNP model, particularly influencing radionuclides generated through neutron capture reactions. Notably, crucial radionuclides for shutdown dose rate calculations in ITER, such as ^{60}Co and ^{58}Co , show a tendency toward slight overestimation, indicating a conservative approach in this comparison.

The analysis also identified large deviations in C/E values for certain isotopes. The introduction of brass depositions through the surface EDM cutting technique explained the discrepancies for ^{65}Zn measurements, while particularly high C/E values (ranging up to 68.4 in a CuCrZr sample) were evident in several foils containing ^{182}Ta . These divergences could arise from inaccuracies in the elemental composition in the associated material certificates and overestimation of the JET MCNP model's thermal flux.

This study highlights how component manufacturing and cutting techniques, such as EDM, can introduce impurities to material surfaces, impacting the generated activities. To study this, some ITER samples underwent surface polishing to remove or eliminate the potential for surface contamination for these subsequent irradiation experiments. These further ITER samples were irradiated within the recently concluded DTE3 experimental campaign, with post-irradiation analysis ongoing and anticipated to complete in late 2024.

In response to the findings to date several actions are proposed, which include conducting independent elemental analysis of ITER samples using techniques such as Inductively Coupled Plasma Optical Emission Spectroscopy (ICP-OES) or Accelerator-based Mass Spectroscopy (AMS). Additionally, leveraging advanced radiometric techniques for both existing and newly irradiated samples from DTE3, reviewing the impacts of diverse sample preparation techniques on impurity introduction, and involving additional ITER material samples in future 14 MeV irradiation experiments are suggested.

This novel and valuable experimental dataset, which is expected to be built upon in the future through further analysis of results from the JET DTE3 experimental campaign, makes a substantial contribution to our comprehension of fusion environments and offers invaluable validation for neutronics methodologies, for example, dose rate assessments during maintenance and radioactive waste arisings on post-operation decommissioning timescales. This work demonstrates that advanced tools such as MCNP and FISPACT-II used with modern nuclear data libraries for neutronics analyses can be reliably applied to predict radionuclide activation in materials exposed to D–T fusion nuclear environments provided that accurate and detailed neutronics models are used and detailed materials certificate information, including impurities, are specified.

Acknowledgment

The authors are particularly grateful for the contribution of the JET operations team, particularly Luke Jones, for their support to this work. In addition, the Materials Research Facility and Health Physics teams at UKAEA were invaluable in facilitating the post-irradiation retrieval activities.

This work has been carried out within the framework of the EUROfusion Consortium, funded by the European Union via the Euratom Research and Training Programme (Grant Agreement No 101052200—EUROfusion), the RCUK Energy Programme (Grant Number EP/W006839/1) and co-financed by the Polish Ministry of Science and Higher

Education within the programme called ‘PMW’ for 2024. Views and opinions expressed are however those of the author(s) only and do not necessarily reflect those of the European Union or the European Commission. Neither the European Union nor the European Commission can be held responsible for them.

ORCID iDs

L.W. Packer  <https://orcid.org/0000-0003-3539-9587>
 M. Fabbri  <https://orcid.org/0000-0002-9979-3025>
 N. Fomesu  <https://orcid.org/0000-0002-2800-0040>
 M.R. Gilbert  <https://orcid.org/0000-0001-8935-1744>
 X. Litaudon  <https://orcid.org/0000-0001-6973-9717>
 M. Pillon  <https://orcid.org/0000-0001-5534-6859>
 M.I. Savva  <https://orcid.org/0000-0003-4238-149X>
 C.R. Shand  <https://orcid.org/0000-0003-2259-8288>

References

- [1] Maggi C. 2024 Overview of T and D-T results in JET with ITER-like Wall *Nucl. Fusion* **64** 112012
- [2] Packer L.W. *et al* 2021 Technological exploitation of the JET neutron environment: progress in ITER materials irradiation and nuclear analysis *Nucl. Fusion* **61** 116057
- [3] Packer L.W. *et al* 2018 Activation of ITER materials in JET: nuclear characterisation experiments for the long-term irradiation station *Nucl. Fusion* **58** 096013
- [4] Packer L. *et al* 2017 Status of ITER material activation experiments at JET *Fusion Eng. Des.* **124** 1150–5
- [5] Zohar A. *et al* 2021 Long term neutron activation in JET DD Operation *EPJ Web Conf.* **253** 03005
- [6] Litaudon X. *et al* 2017 Overview of the JET results in support to ITER *Nucl. Fusion* **57** 102001
- [7] Litaudon X. *et al* 2024 EUROfusion contributions to ITER nuclear operation *Nucl. Fusion* **64** 112006
- [8] Mailloux J. *et al* 2022 Overview of JET results for optimising ITER operation *Nucl. Fusion* **62** 042026
- [9] Batistoni P. *et al* 2016 Technological exploitation of Deuterium–Tritium operations at JET in support of ITER design, operation and safety *Fusion Eng. Des.* **109** 278–85
- [10] Batistoni P. *et al* 2017 14 MeV calibration of JET neutron detectors-phase 1: calibration and characterization of the neutron source *Nucl. Fusion* **58** 026012
- [11] Batistoni P. *et al* 2018 14 MeV calibration of JET neutron detectors-phase 2: in-vessel calibration *Nucl. Fusion* **58** 106016
- [12] Laszynska E. *et al* 2019 In-vessel calibration of JET neutron detectors: comparison of methods of neutron emission rate determination *Fusion Eng. Des.* **146** 1661–4
- [13] Villari R. *et al* 2016 Neutronics experiments and analyses in preparation of DT operations at JET *Fusion Eng. Des.* **109** 895–905
- [14] Villari R. *et al* 2017 ITER oriented neutronics benchmark experiments on neutron streaming and shutdown dose rate at JET *Fusion Eng. Des.* **123** 171–6
- [15] Obryk B., Batistoni P., Conroy S., Syme B.D., Popovichev S., Stamatelatos I.E., Vasilopoulou T. and Bilski P. 2014 Thermoluminescence measurements of neutron streaming through JET Torus Hall ducts *Fusion Eng. Des.* **89** 2235–40
- [16] Batistoni P. *et al* 2015 Benchmark experiments on neutron streaming through JET Torus Hall penetrations *Nucl. Fusion* **55** 053028
- [17] Vasilopoulou T., Stamatelatos I., Batistoni P., Conroy S., Obryk B., Popovichev S. and Syme D. 2015 Neutron streaming along ducts and labyrinths at the JET biological shielding: effect of concrete composition *Radiat. Phys. Chem.* **116** 359–64
- [18] Vasilopoulou T. *et al* 2019 Activation foil measurements at jet in preparation for D-T plasma operation *Fusion Eng. Des.* **146** 250–5
- [19] Naish J.D. *et al* 2021 Comparison of neutron flux streaming calculations to the 2019–2020 JET Experimental Deuterium–Deuterium Results *Fusion Eng. Des.* **170** 112538
- [20] Nobs C. *et al* 2019 Neutron spectrum unfolding for the development of a novel neutron detector for fusion *Fusion Eng. Des.* **146** 2658–62
- [21] Colling B.C. *et al* 2017 Testing of tritium breeder blanket activation foil spectrometer during JET operations *Fusion Eng. Des.* **136** 258–64
- [22] Martone M., Angelone M. and Pillon M. 1994 The 14 MeV Frascati neutron generator *J. Nucl. Mater.* **212–215** 1661–4
- [23] Maekawa F. and Ikeda Y. 2000 Decay heat experiment on thirty-two fusion reactor relevant materials irradiated by 14-MeV neutrons *Fusion Eng. Des.* **47** 377–88
- [24] Packer L., Gilbert M., Hughes S., Lilley S., Pampin R. and Sublet J.-C. 2012 UK fusion technology experimental activities at the ASP 14 MeV neutron irradiation facility *Fusion Eng. Des.* **87** 662–6
- [25] Kodeli I.A. and Sartori E. 2021 Sinbad – radiation shielding benchmark experiments *Ann. Nucl. Energy* **159** 108254
- [26] Schnabel G. *et al* 2024 FENDL: a library for fusion research and applications *Nucl. Data Sheets* **193** 1–78
- [27] Sublet J.-C., Eastwood J.W. and Morgan J.G. 2014 The FISPACT-II User Manual *Technical Report CCFE-R(11) 11 Issue 6 CCFE*
- [28] Sublet J.-C., Eastwood J., Morgan J., Gilbert M., Fleming M. and Arter W. 2017 FISPACT-II: an advanced simulation system for activation, transmutation and material modelling *Nucl. Data Sheets* **139** 77–137
- [29] Pelowitz D.B. *et al* 2013 MCNP6 user’s manual version 1 *Los Alamos document number: LA-CP-13-00634 Rev. 0*
- [30] Gilbert M.R., Sublet J.-C. and Turner A. 2016 Handbook of activation, transmutation, and radiation damage properties of the elements and of ITER materials simulated using FISPACT-II & TENDL-2015; ITER FW armour focus *Technical Report CCFE-R(16)37*
- [31] Barabash V. 2016 Chemical compositions of materials representing the components included into basic model for nuclear analysis of ITER, IO, ITER-D-HTN8X3 V2.1, 1
- [32] Savva M.I. *et al* 2021 Application of VERDI detectors for neutron fluence measurements during the JET 2019 Deuterium–Deuterium campaign *Fus. Eng. Des.* **166** 112286
- [33] Riccardi B., Gavila P., Andrade J., Escourbiac F., Fedosov A., Durocher A. and Kuznetsov V. 2019 Progress of the EU activities for the ITER divertor inner vertical target procurement *Fusion Eng. Des.* **146** 1524–7
- [34] Knoll G. 2010 *Radiation Detection and Measurement* 4th edn (Wiley)
- [35] Werner J.C. *et al* 2018 MCNP Version 6.2 Release Notes
- [36] Schnabel G., Capote R. and Trkov A. 2024 Fusion Evaluated Nuclear Data Library - IAEA (available at: www-nds.iaea.org/fendl/)
- [37] Mosher S. *et al* 2015 ADVANTG—an automated variance reduction parameter generator, *Technical Report ORNL/TM-2013/416 Rev. 1*, Oak Ridge National Laboratory, Oak Ridge, TN

- [38] Trkov A. *et al* 2020 IRDFF-II: a new neutron metrology library *Nucl. Data Sheets* **163** 1–108
- [39] Packer L. *et al* 2020 Neutron detection and measurement challenges at JET and ITER *Modern Neutron Detection, IAEA-TECDOC-1935*, Ed I. Swainson (International Atomic Energy Agency) pp 313–35
- [40] JET neutron yield data EUROfusion IDM report 2023 EFDA_D_2QNZ84
- [41] M. Herman and A. Nichols (eds) 2007 Update of x ray and gamma ray decay data standards for detector calibration and other applications vol 1 (International Atomic Energy Agency) (available at: www-pub.iaea.org/MTCD/publications/PDF/Pub1287_Vol2_web.pdf)